การผลิตไฮโดรเจนจากการเปลี่ยนรูปด้วยไอน้ำของเอทานอล บนตัวเร่งปฏิกิริยาฐานนิกเกิลรองรับบนซีเรีย

นายฮวง แนม ตรัน ดัง

วิทยานิพนธ์นี้เป็นส่วนหนึ่งของการศึกษาตามหลักสูตรปริญญาวิทยาศาสตรมหาบัณฑิต
สาขาวิชาเคมีเทคนิค ภาควิชาเคมีเทคนิค
คณะวิทยาศาสตร์ จุฬาลงกรณ์มหาวิทยาลัย
ปีการศึกษา 2558

HYDROGEN PRODUCTION FROM ETHANOL STEAM REFORMING OVER NICKEL–BASED CATALYSTS SUPPORTED ON CERIA

Mr. Huan Nam Tran Dang

A Thesis Submitted in Partial Fulfillment of the Requirements
for the Degree of Master of Science Program in Chemical Technology
Department of Chemical Technology
Faculty of Science
Chulalongkorn University
Academic Year 2015

Thesis Title	HYDROGEN PRODUCTION FROM ETHANOL STEAM REFORMING OVER NICKEL–BASED CATALYSTS SUPPORTED ON CERIA
By	Mr. Huan Nam Tran Dang
Field of Study	Chemical Technology
Thesis Advisor	Associate Professor Nattaya Pongstabodee, Ph.D.

Accepted by the Faculty of Science, Chulalongkorn University in Partial Fulfillment of the Requirements for the Master's Degree

.....Dean of the Faculty of Science
(Associate Professor Polkit Sangvanich, Ph.D.)

THESIS COMMITTEE

.....Chairman
(Assistant Professor Prasert Reubroycharoen, Ph.D.)

.....Thesis Advisor
(Associate Professor Nattaya Pongstabodee, Ph.D.)

.....Examiner
(Associate Professor Chawalit Ngamcharussrivichai, Ph.D.)

.....External Examiner
(Siriphong Rojluechai, Ph.D.)

ฮวง แนม ตรัน ดัง : การผลิตไฮโดรเจนจากการเปลี่ยนรูปด้วยไอน้ำของเอทานอลบนตัวเร่งปฏิกิริยาฐานนิกเกิลรองรับบนซีเรีย (HYDROGEN PRODUCTION FROM ETHANOL STEAM REFORMING OVER NICKEL–BASED CATALYSTS SUPPORTED ON CERIA) อ.ที่ปรึกษาวิทยานิพนธ์หลัก: รศ. ดร.ณัฐธยาน์ พงศ์สถาบดี, 83 หน้า.

วัตถุประสงค์ของงานวิจัยนี้ คือเพื่อตรวจสอบประสิทธิภาพการเร่งปฏิกิริยาของตัวเร่งปฏิกิริยานิกเกิลที่รองรับบนซีเรียสำหรับการผลิตกระแสไฮโดรเจนเข้มข้นผ่านกระบวนการรีฟอร์มมิ่งของเอทานอลด้วยไอน้ำ งานวิจัยนี้แบ่งออกเป็นสองส่วน ในส่วนแรกจะทำการสังเคราะห์ตัวเร่งปฏิกิริยานิกเกิลด้วยกันสามชุดที่ปริมาณโลหะแตกต่างกันและรองรับบนซีเรียชนิดผลึกรวมธรรมดา ได้แก่ Ni-Mn/CeO_2-P Ni-Cu/CeO_2-P และ Ni-Cu-Mn/CeO_2-P ประสิทธิภาพการเร่งปฏิกิริยาของตัวอย่างเหล่านี้ในรีฟอร์มมิ่งของเอทานอลด้วยไอน้ำได้ดำเนินการตรวจสอบภายใต้ความดันบรรยากาศ อุณหภูมิปฏิกิริยา 400 องศาเซลเซียส อัตราส่วนไอน้ำต่อเอทานอล เท่ากับ 3 และอัตราส่วนน้ำหนักตัวเร่งปฏิกิริยาต่ออัตราการไหลของแก๊สโดยรวม เท่ากับ 22.44 กรัม ชั่วโมงต่อโมล ผลการศึกษาพบว่าตัวเร่งปฏิกิริยาที่มีปริมาณทองแดงสูงให้ผลได้ของไฮโดรเจนที่มาก แต่กลับทำให้เกิดผลพลอยได้ที่เป็นอันตรายในปริมาณมาก ประกอบด้วย CO CH_3CHO CH_3COCH_3 และ C_2H_4 ตัวเร่งปฏิกิริยา 10Mn90Ni/CeO_2-P เป็นตัวเร่งปฏิกิริยาที่ดีที่สุดในแง่ของการเปลี่ยนเอทานอล ผลได้ของไฮโดรเจน และการกระจาย ของผลิตภัณฑ์ที่ได้ ในส่วนที่สองจะนำปริมาณนี้ไปใช้ซึ่งเมทริกซ์ทางสถิติของการทดลอง ที่ระดับความเชื่อมั่นร้อยละ 95 ใช้ในการกำหนดปัจจัยที่สำคัญและเพื่อหาสภาวะที่เหมาะสม สำหรับผลได้ของไฮโดรเจนสูงสุด ผลลัพธ์ที่ได้จากการออกแบบ 2^4 แฟ็คทอเรียลที่มี 4 จุดกลางทำให้ทราบว่า การดำเนินการทดลอง ณ อุณหภูมิปฏิกิริยาที่สูงและอัตราส่วนไอน้ำต่อเอทานอลที่สูงโดยใช้ตัวเร่งปฏิกิริยาที่รองรับบนซีเรียชนิดแท่งนาโนจะมีเป็นประโยชน์สำหรับการผลิตไฮโดรเจน ผลได้รับของไฮโดรเจนสูงสุดร้อยละ 43.1 ที่อุณหภูมิปฏิกิริยา 600 องศาเซลเซียส อัตราส่วนไอน้ำต่อเอทานอล เท่ากับ 7 และตัวเร่งปฏิกิริยาด้วยที่มีซีเรียชนิดแท่งนาโนเป็นตัวรองรับ

ภาควิชา เคมีเทคนิค ลายมือชื่อนิสิต .....

สาขาวิชา เคมีเทคนิค ลายมือชื่อ อ.ที่ปรึกษาหลัก .....

ปีการศึกษา 2558

5772234423 : MAJOR CHEMICAL TECHNOLOGY

KEYWORDS: ETHANOL STEAM REFORMING,FACTORIAL DESIGN, CERIA, MORPHOLOGY, NICKEL-BASED CATALYSTS

HUAN NAM TRAN DANG: HYDROGEN PRODUCTION FROM ETHANOL STEAM REFORMING OVER NICKEL–BASED CATALYSTS SUPPORTED ON CERIA. ADVISOR: ASSOC. PROF. NATTAYA PONGSTABODEE, Ph.D., 83 pp.

The objective of this work is to investigate the catalytic performance of nickel-based catalyst supported on ceria for producing hydrogen-rich stream via ethanol steam reforming. This work was divided into two phases. In the first phase, three series of nickel-based catalysts with different metal loadings supported on conventional polycrystalline ceria, Ni-Mn/CeO_2-P, Ni-Cu/CeO_2-P and Ni-Cu-Mn/CeO_2-P, were synthesized. The catalytic performance of those samples in ethanol steam reforming under atmospheric pressure, reaction temperature of 400^{o}C, S/E ratio of 3 and W/F ratio of 22.44g_{cat}h/$mole_{ethanol}$ was examined. The results revealed that catalysts with high copper content gave considerable hydrogen yield, but expressed strong preference for detrimental byproducts including CO, CH_3CHO, CH_3COCH_3 and C_2H_4. 10Mn90Ni/CeO_2-P was the best catalyst in terms of ethanol conversion, hydrogen yield and product distribution. This loading was then applied for the second phase, where a statistical matrix of experiments at a 95% confidence interval to determine significant factors and to find optimum conditions for maximal hydrogen yield. Results from 2^4 factorial design with 4 central points revealed that conducting experiments at high reaction temperatures and high S/E molar ratio using catalysts supported on ceria nanorods would be beneficial for hydrogen production. The maximum hydrogen yield obtained was 43.1% at temperature of 600^{o}C, S/E ratio of 7 and catalysts with ceria nanorods support.

Department: Chemical Technology Student's Signature .....

Field of Study: Chemical Technology Advisor's Signature .....

Academic Year: 2015

ACKNOWLEDGEMENTS

I would like to express my profound gratitude to my advisor, Associate Professor Dr. Nuttaya Pongstabodee, for her tremendous support and encouragement, without which I would not have been able to complete this work. Her valuable advice has enormously helped me to overcome difficulty in adapting to the new study environment. I am also grateful to other lecturers who provided me with basic knowledge during the first year. Besides, I would also like to thank all of my friends, especially Mr. Yuththaphan Phongboonchoo for his considerable assistance in analyzing some properties of my catalysts.

In addition, without financial support from the ASEAN Scholarship fund, I would not have had the chance to experience excellent higher education in Chulalongkorn University. Special thanks go to Assistant Professor Dr. Prasert Reubroycharoen for introducing this scholarship to me. I would like to show my deep appreciation to the Graduate School of Chulalongkorn University for all its support during the past two years. Last but not least, there are no words to describe how grateful I am to my parents for all sacrifices they made so that I could have a good education.

CONTENTS

Page

Page

Page

LIST OF TABLES

LIST OF FIGURES

CHAPTER 1: INTRODUCTION

1.1. Motivations

The wide – scale extraction and over exploitation of natural resources have resulted in a number of negative effects, chief among which are the dramatic decrease in fossil fuels and the greater level of environmental contamination. To deal with these urgent problems, clean alternative sources of energy should be developed to reduce our dependence on petroleum–based fuels. In this regard, hydrogen (H_2), considered as a secondary source of energy or more commonly referred to as an energy carrier, is supposed to play a vital role in the energy systems of the future because it could be generated from several renewable sources and converted into energy with high efficiency.

There are numerous advantages of utilizing hydrogen in terms of an important energy carrier. For example, a large volume of hydrogen can be easily stored in a number of different ways. Hydrogen is also a low polluting fuel that can be used for transportation, heating, and power generation in places where it is difficult to use electricity. In some instances, it is cheaper to ship hydrogen by pipeline than sending electricity over long distances by wire.

Since hydrogen does not exist on Earth as a gas, it must be separated from other compounds. Two of the most common methods used for the production of hydrogen are electrolysis or water splitting and steam reforming, but the latter approach is currently the least expensive one. It is used in industries to separate hydrogen atoms from carbon atoms in methane. However, the main drawback of this production is that methane is a fossil fuel, and such non-renewable source should not be further exploited in order to partly reduce the rapid depletion of fuels formed by natural processes. The use of hydrogen produced from bio–derived liquids, therefore, would be of great interest as a tremendous potential source of sustainable energy. Among the viable options for generating hydrogen from biomass, ethanol steam reforming (ESR) has emerged as one of the most promising

approaches due to non–toxic character, high availability, relatively low cost of ethanol and the great H_2 yield of the reforming process [1, 2].

Hydrogen can be yielded from ethanol owing to some catalytic reactions during the steam reforming process, but the profitability of the entire process crucially depends on the catalyst selection. Indeed, the catalyst has an essential part in increasing the rate of reaction in such a way that the system tends towards thermodynamic equilibrium [3, 4]. The ethanol steam reforming reaction can be catalyzed by noble and non–noble metals supported on different oxides. Rh and Pt are the noble metals that have been extensively studied and exhibited remarkable activity and stability [5, 6]. Although high activity was shown by these catalysts, high cost associated with such catalytic systems would limit their application to large–scale schemes. Apart from noble metal catalysts, non–noble metal catalysts have also been investigated and used for ethanol steam reforming. Interestingly, supported transition metals catalysts (Ni, Co, Cu) present similar activity to that acquired from noble metal counterparts under some specific conditions [7-9].

This thesis can be divided into two phases. The first phase is called "Identifying" where 3 series of catalysts, Ni-Mn, Ni-Cu, and Ni-Cu-Mn supported on conventional polycrystalline ceria, would be tested under fixed conditions of ethanol steam reforming to find out the catalyst having the best activity with regard to ethanol conversion, H_2 yield, and the amounts of undesired products.

Subsequently, the other phase, "Measuring", would be to examine the performance of the best catalyst from the previous phase under different parameters based on a full 2^k factorial design.

1.2. Objectives

The objective of this work is to investigate the influence of various parameters on the activity of nickel–based catalyst supported on ceria for producing hydrogen–rich stream via ethanol steam reforming.

1.3. Scope of the research

To achieve the objective of this research, the following procedure will be adopted:

1) Literature review

2) Catalysts preparation: ceria will be synthesized by precipitation and hydrothermal method. After that the active phase will be loaded onto ceria via incipient wetness impregnation.

3) Catalytic activity tests:

Catalysts with different metal loadings supported on conventional polycrystalline ceria will be synthesized and subsequently tested the ESR activity to find out the optimal catalyst under a specific reaction condition. These optimal loadings of Ni, Cu and Mn will be applied to other morphologies of ceria, namely nanorods, nanocubes and nanoparticles to inspect their impact on catalytic performance of the ESR reaction.

The catalyst with the best activity will undergo the ESR reaction under different parameters:

- Temperature: 400, 500 & 600°C
- Steam to ethanol (S/E) ratio: 3, 5 & 7
- Weight of catalysts to feed rate of ethanol (W/F_{EtOH}): 7,48, 14.96 & 22.44 $g_{cat}h$/mole [EtOH]
- Ceria morphologies: conventional polycrystalline, nanorods & nanocubes

The gaseous effluent (H_2, CO, CO_2, CH_4, C_2H_4) will be analyzed online using a Shimadzu GC 2014 gas chromatography with Shincarbon column via TCD detector, whereas the liquid products (C_2H_5OH, CH_3CHO, CH_3COCH_3) needs another GC equipped with DB Wax column and FID detector.

3) Catalyst characterization

- X-ray diffraction (XRD) for structural analysis of catalysts.
- Temperature programmed reduction (TPR) for reduction behavior analysis of catalysts.
- Transmission electron microscopy (TEM) for determining particle size, surface characteristics and heterogeneity observation of catalysts.
- Nitrogen adsorption/desorption for BET surface areas and pore volume of catalysts.
- Thermogravimetric analysis (TGA) of spent catalysts for measuring the amount of coke removal from catalysts surface.

4) Discussing the results and writing the thesis

1.4. Expectations

The combination of the role of each parameter studied in the hydrogen production via ESR and the ESR optimization under statistical design are hoped to bring the catalyst with high activity and stability.

CHAPTER 2: THEORY AND LITERATURE REVIEW

2.1. Important reactant and desired product

2.1.1. Reactant: ethanol

Ethanol is a clear, volatile, flammable, colorless liquid with a slight chemical odor. It is also known as ethyl alcohol, grain alcohol, and EtOH. Ethanol has the same chemical formula regardless of whether it is produced from starch- and sugar-based feed-stocks, such as corn grain, sugar cane, or from cellulosic feed-stocks (such as wood chips or crop residues). It is used as an antiseptic, a solvent, a fuel, and due to its low freezing point, the active fluid in many alcohol thermometers. The molecule is a simple one, being an ethyl group linked to a hydroxyl group. Its structural formula, CH_3CH_2OH, is often abbreviated as C_2H_5OH, C_2H_6O or EtOH. Information about typical properties of ethanol is given in Table 1 below.

Table 1: Typical properties of ethanol

Property	Corresponding value/characteristic
Chemical formula	C_2H_6O
Molar mass	46.07 g/mol
Density	0.789 g/cm^3 (at 20°C)
Melting point	−114°C (−173°F; 159K)
Boiling point	78.37°C (173.07°F; 351.52K)
Solubility in water	Miscible
Vapor pressure	5.95 kPa (at 20°C)
Acidity (pK_a)	15.9 (H_2O), 29.8 (DMSO)
Basicity (pK_b)	−1.9
Refractive index (n_D)	1.361
Viscosity	1.2 mPa.s (at 20°C), 1.074 mPa.s (at 25°C)
Dipole moment	1.69 D

2.1.2. Desired product: hydrogen

Hydrogen is a chemical element with chemical symbol **H** and atomic number 1. With an atomic weight of 1.00794 u, hydrogen is the lightest element on the periodic table. At standard temperature and pressure, hydrogen is a colorless, odorless, tasteless, non-toxic, nonmetallic, highly combustible diatomic gas with the molecular formula H_2. Since hydrogen readily forms covalent compounds with most non-metallic elements, most of the hydrogen on Earth exists in molecular forms such as water or organic compounds. Some characteristics of this gas are presented in Table 2 below.

Table 2: Typical properties of hydrogen

Property	**Corresponding value/characteristic**
Chemical formula	H_2
Color	Colorless
Phase	Gas
Melting point	13.99K (−259.16°C, −434.49°F)
Boiling point	20.271K (−252.879°C, −423.182°F)
Triple point	13.8033 K, 7.041 kPa
Critical point	32.938 K, 1.2858 MPa
Heat of fusion	(H_2) 0.117 kJ/mol
Heat of vaporization	(H_2) 0.904 kJ/mol
Molar heat capacity	(H_2) 28.836 J/(mol·K)

Hydrogen has a wide variety of applications, but the one that has been attracting special attention of researchers is to use it as a clean fuel of the future. Hydrogen-powered fuel cells are increasingly being seen as “pollution-free” sources of energy and are now being used in some buses and cars. It is an environmentally friendly fuel that has the potential to dramatically reduce our dependence on

natural resources, but several significant challenges must be overcome before it can be widely used. One of the challenges of using hydrogen as a fuel comes from being able to efficiently extract hydrogen from other compounds such as water, hydrocarbons and other organic matter. Hydrogen can also be produced from water through electrolysis, but this method is much more energy intensive. Instead, steam reforming has proved more efficient in producing hydrogen since it requires less energy and the supply of feed is more plentiful. Renewable sources of energy, such as wind or solar, can be used as the energy source to produce hydrogen, avoiding harmful emissions from other kinds of energy production.

2.2. Hydrothermal method

Hydrothermal method includes the various techniques of crystallizing substances from high-temperature aqueous solutions at high vapor pressures; also termed "hydrothermal synthesis". Hydrothermal synthesis can be defined as a method of synthesis of single crystals that depends on the solubility of minerals in hot water under high pressure. The crystal growth is performed in an apparatus consisting of a steel pressure vessel called an autoclave, in which a nutrient is supplied along with water. A temperature gradient is maintained between the opposite ends of the growth chamber. At the hotter end the nutrient solute dissolves, while at the cooler end it is deposited on a seed crystal, growing the desired crystal. Advantages of the hydrothermal method over other types of crystal growth include the ability to create crystalline phases which are not stable at the melting point. Also, materials which have a high vapor pressure near their melting points can be grown by the hydrothermal method. The method is also particularly suitable for the growth of large good-quality crystals while maintaining control over their composition. Disadvantages of the method include the need of expensive autoclaves, and the impossibility of observing the crystal as it grows.

The crystallization vessels used are autoclaves. These are usually thick-walled steel cylinders with a hermetic seal which must withstand high temperatures and pressures for prolonged periods of time. Furthermore, the autoclave material must be inert with respect to the solvent. The closure is the most important

element of the autoclave. Many designs have been developed for seals, the most famous being the Bridgman seal. In most cases, steel-corroding solutions are used in hydrothermal experiments. To prevent corrosion of the internal cavity of the autoclave, protective inserts are generally used. These may have the same shape as the autoclave and fit in the internal cavity (contact-type insert), or be a "floating" type insert which occupies only part of the autoclave interior. Inserts may be made of carbon-free iron, copper, silver, gold, platinum, titanium, glass (or quartz), or Teflon, depending on the temperature and solution used. For this research, the insert was a Teflon-lined cylinder, and this method was utilized to prepare ceria with different morphologies, namely nanocubes and nanorods. The specific procedure when applying hydrothermal method would be described in section 3.4.

2.3. Theory of steam reforming of ethanol

2.3.1. Chemistry

The reaction pathways and thermodynamics of ethanol steam reforming have been studied extensively recently, which the classic route is described in equation (1):

$$CH_3CH_2OH\ (g) + 3H_2O\ (g) \rightarrow 6H_2\ (g) + 2CO_2\ (g) \qquad (1)$$

The SRE process involves the reaction between ethanol and water over a metal catalyst capable of breaking the C – C bond in ethanol to produce a mixture of H_2 and CO_2. The reaction is highly endothermic with a standard enthalpy, $\Delta H^{o}_{298} = +173.3 kJ/mol$ of ethanol and occurs at relatively higher temperatures, typically between 300 and 800°C.

$$CH_3CH_2OH\ (g) + H_2O\ (g) \rightarrow 4H_2\ (g) + 2CO\ (g) \qquad (2)$$

$$CO\ (g) + H_2O\ (g) \rightarrow CO_2\ (g) + H_2\ (g) \qquad (3)$$

$$CH_3CH_2OH\ (g) \rightarrow H_2\ (g) + CO\ (g) + CH_4\ (g) \qquad (4)$$

This reaction is considered as a combination of SRE to syngas (Eq. 2) followed by water gas shift reaction (WGS) (Eq. 3). Many other reactions, however, can occur simultaneously with hydrogen production reactions depicted above (Eqs

(1)–(4)), which results in several side products. Those reactions, for example, can be enumerated in the Table 3 below. In addition, both reaction conditions and catalysts used significantly affect those reaction pathways, which will be briefly illustrated.

Table 3: Other possible reaction pathways of ethanol steam reforming [2, 3]

Reaction	Equation
Ethanol hydrogenolysis to methane	$C_2H_5OH + 2H_2 \longrightarrow 2CH_4 + H_2O$
Ethanol dehydration to ethylene	$C_2H_5OH \longrightarrow C_2H_4 + H_2O$
Ethanol dehydrogenation to acetaldehyde	$C_2H_5OH \longrightarrow C_2H_4O + H_2$
Acetaldehyde decomposition to CH_4 and CO	$C_2H_4O \longrightarrow CH_4 + CO$
Acetaldehyde steam reforming	$C_2H_4O + H_2O \longrightarrow 3H_2 + 2CO$
Acetone formation	$2C_2H_5OH \longrightarrow C_3H_6O + CO + 3H_2$
Methane steam reforming	$CH_4 + H_2O \longrightarrow CO + 3H_2$
Methanation	$CO + 3H_2 \longrightarrow CH_4 + H_2O$
Methane decomposition	$CH_4 \longrightarrow 2H_2 + C$
Boudouard reaction	$2CO \longrightarrow CO_2 + C$
Coke formation	$C_2H_4 \longrightarrow$ polymeric deposits (coke)

2.3.2. Factors influencing reaction pathways

2.3.2.1. Reaction temperature

As the reforming process is highly endothermic, higher reaction temperatures will favor the ethanol conversion. Figure 1 shows that reactions of ethanol such as ethanol dehydrogenation, ethanol dehydration, and ethanol decomposition are thermodynamically promoted at high temperatures. Another aspect of the process that is also influenced by the reaction temperature is the product distribution. When increasing the temperature, the selectivity towards CO_2

and CH_4 decreases, while that of H_2 and CO mounts. As can be seen from Figure 2, methane and other intermediates such as acetaldehyde and ethylene will be consumed via the steam reforming reactions, thereby decreasing the concentrations of those agents.

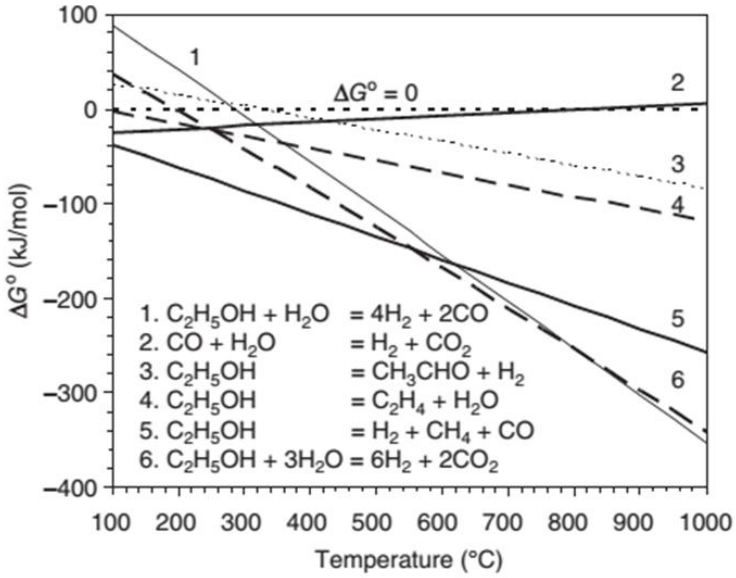

Figure 1: : Free energy changes in the steam reforming, decomposition, dehydrogenation, and dehydration of ethanol. The data for water - gas shift reaction are also included [4].

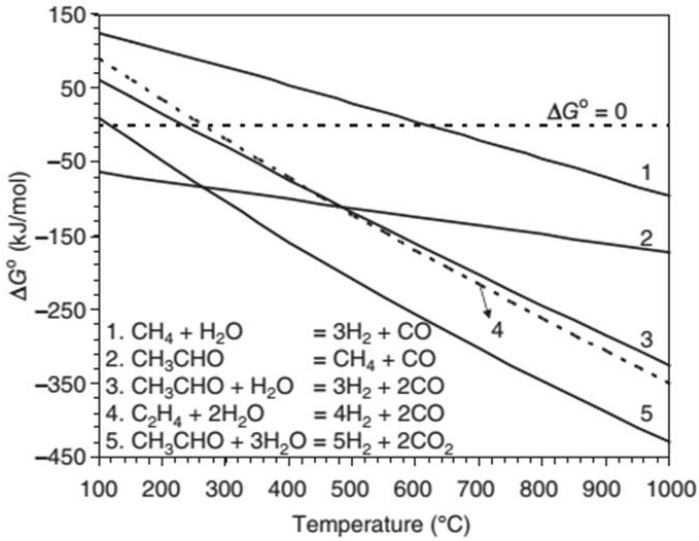

Figure 2: Free energy changes in the steam reforming of acetaldehyde, ethylene, and methane [4].

2.3.2.2. Steam to ethanol molar ratio

Apart from the reaction temperature, this also plays a pivotal role in ethanol conversion and product distribution. Although a steam-to-ethanol (H_2O/EtOH) molar ratio of 3 is stoichiometrically required, other authors have conducted the ESR using higher steam to ethanol molar ratios and have reported that excessive amounts of water would be beneficial to ethanol conversion [3, 4, 10-14]. In terms of product distribution, the quantities of H_2 and CO_2 would dramatically rise with increasing H_2O/EtOH ratio, whereas the concentrations of CO and CH_4 would be reduced. This can be explained by the fact that water encourages steam reforming reactions of agents such as methane and intermediates, as mentioned above, and shifts the WGS equilibrium forward to convert CO into CO_2 and produce additional amount of H_2. Nevertheless, the use of high H_2O/EtOH molar ratios in the reforming process will be limited by the energy cost of the system since a higher H_2O/EtOH molar ratio means extra steam to be generated [9].

2.3.2.3. Residence time

It has been reported that residence time is directly proportional to the conversion of ethanol and H_2 formation [3, 11]. Authors explained that ethanol decomposition would be promoted at low residence times, whereas the reforming of byproducts such as acetaldehyde and ethylene did not take place under such condition.

2.3.2.4. Catalysts

As mentioned before, the ESR process involves a wide variety of reversible reactions, and the hydrogen production, as well as induced reactions pathways, largely counts on the selection of a proper catalyst. While catalysts with supported noble metals give extraordinary performance, enormous cost is the major drawback of utilizing those catalysts in industrial scale. In order to solve this problem, it is urgent to find a feasible replacement which can satisfy both activity and economic requirements. Among the possible solutions, Ni is a very common and effective active phase for the ESR reaction when it comes to catalytic activity and

hydrogen selectivity. In addition, the good ability to rupture the C – C bond and low cost make Ni an auspicious replacement for noble metals. Chitsazan et al. [15] studied the steam reforming of biomass-derived organics over catalysts based on Ni/Al_2O_3 and found that the 16% Ni/Al_2O_3 sample had high activity for ethanol steam reforming under conditions as follows: the reaction temperature of 973K, the feed was comprised of ethanol and water with a molar ratio (water to ethanol) equal to 6 in He (41.6% mol/mol), and gas hourly space velocity of $51700h^{-1}$. The conversion and hydrogen yield obtained over this catalyst were 100% and 63%, respectively.

However, shortcomings are inevitable when Ni–based catalysts are utilized such as rapid deactivation tendency due to high coke deposition. As a result, modifications are required to maintain long–term stability of catalysts based on Ni metal. There are several methods to fulfill this task, one of which is adding rare earth oxide promoters (CeO_2 and La_2O_3) to the typical Ni/γ - Al_2O_3 catalyst [16] or even replacing the γ - Al_2O_3 having high acidity with other oxide supports [7]. Some authors have reported that Mn-doped CeO_2–ZrO_2 supported nickel catalysts displayed good activity for naphthalene steam reforming and the amount of carbon deposition reduced substantially when Mn was introduced to the CeO_2–ZrO_2 mixed oxide [17]. This finding could be applied to the case of ESR as a different pathway to tackle coke issues.

Besides the performance of the active agent, the nature of the metal oxide support has been found to occupy a crucial role in the ESR reaction. γ - Al_2O_3 is a common support for steam reforming catalysts owing to its high surface area, thermal and chemical stability under reforming conditions. Nevertheless, high surface acidity of γ - Al_2O_3 could produce ethylene, which can be easily dehydrogenated to form coke over metal phases. For that reason some researchers (Divins et al. [18], Soykal et al. [19], Moraes et al. [20]) have switched to other supports such as CeO_2 and have collected satisfactory results. The advantages of CeO_2 are attributed to its higher reducibility in the presence of noble metals, the improvement of metal active particles dispersion and the prevention of sintering of metal particles.

2.4. Experimental design

In an experiment, we deliberately change one or more process variables (or factors) in order to observe the effect the changes have on one or more response variables. The (statistical) design of experiments (DOE) is an efficient procedure for planning experiments so that the data obtained can be analyzed to yield valid and objective conclusions.

DOE begins with determining the objectives of an experiment and selecting the process factors for the study. An Experimental Design is the laying out of a detailed experimental plan in advance of doing the experiment. Well-chosen experimental designs maximize the amount of "information" that can be obtained for a given amount of experimental effort. The statistical theory underlying DOE generally begins with the concept of process models.

Process Models for DOE

It is common to begin with a process model of the “black box' type”, with several discrete or continuous input factors that can be controlled-that is, varied at will by the experimenter-and one or more measured output responses. The output responses are assumed continuous. Experimental data are used to derive an empirical (approximation) model linking the outputs and inputs. These empirical models generally contain first and second-order terms. Often the experiment has to account for a number of uncontrolled factors that may be discrete, such as different machines or operators, and/or continuous such as ambient temperature or humidity. Figure 3 illustrates this situation.

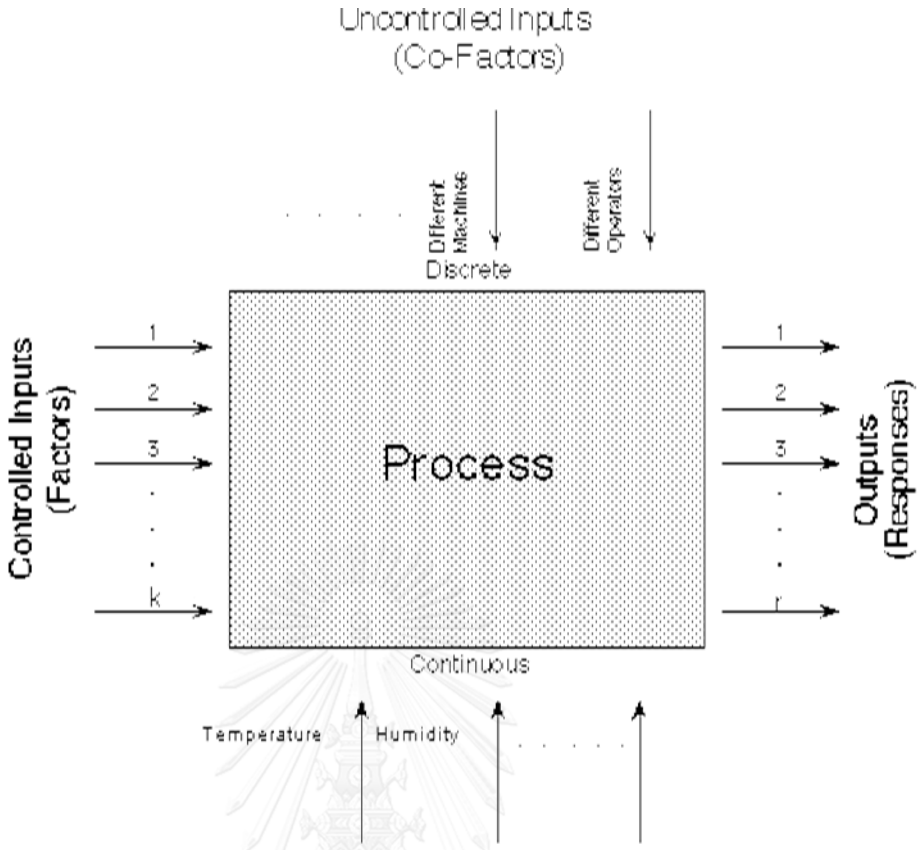

Figure 3: A "Black Box" Process Model Schematic

The most common empirical models fit to the experimental data take either a *linear* form or *quadratic* form. A linear model with two factors, x_1 and x_2, can be written as follows:

$$y = \beta_o + \beta_1 x_1 + \beta_2 x_2 + \beta_{12} x_1 x_2 + \varepsilon$$

Here, y is the response for given levels of the main effects x_1 and x_2 and the x_1x_2 term is included to account for a possible interaction effect between x_1 and x_2. The constant β_o is the response of y when both main effects are 0, and ε is a random error term that accounts for the experimental error in the system that is being studied. Higher-order interactions can also be included in experiments with more than two factor if necessary. Another widely used model is the second-order model

$$y = \beta_o + \beta_1 x_1 + \beta_2 x_2 + \beta_{12} x_1 x_2 + \beta_{11} x_{11}^2 + \beta_{22} x_{22}^2 + \varepsilon$$

Second-order models are often used in optimization experiments.

Performing the experiment

When running the experiment, it is vital to monitor the process carefully to ensure that everything is being done according to the plan. Errors in experimental procedure at this stage will usually destroy experimental validity.

Statistical analysis of the data

Statistical methods should be used to analyze the data so that the results and conclusions are objective rather than judgmental in nature. If the experiment has been designed correctly and performed according to the design, the statistical methods required are not elaborate. Often graphical methods play an important role in data analysis and interpretation. Because many of the questions that the experimenter wants to answer can be cast into an hypothesis-testing framework, hypothesis testing and confidence interval estimation procedures are very helpful in analyzing the data from a designed experiment. It is also usually useful to present the results of many experiments in terms of an empirical model, that is, an equation derived from the data that express the relationship between the response and the important design factors. Residual analysis and model adequacy checking are also important analysis techniques.

Conclusions and recommendations

Once the data have been analyzed, the experimenter must draw practical conclusions about the results and recommend a course of action. Graphical methods are often useful in this stage, particularly in presenting the results to others. Follow up runs and confirmation testing should also be performed to validate the conclusions from the experiment.

2.5. Literature review

In 2001, Marino et al. [21] investigated catalytic performance of Cu-Ni-K/γ-Al_2O_3 catalysts for ESR at 300^{o}C, steam to ethanol molar ratio of 2.5:1, and LHSV of 1.8h^{-1}. The authors found that copper was responsible for gasifying ethanol, and that nickel possessed high C-C bond cleavage activity. Specifically, when adding nickel to the Cu/γ-Al_2O_3 catalysts, the gas yield rose remarkably with the increase of Ni content. In particular, the amount of gas produced from the catalyst containing 6 wt% copper and 6 wt% nickel was approximately 2.5 times higher than that derived from the copper-only sample. This is likely due to the ability of nickel to break the C-C bonds present in condensable products (CH_3CHO and CH_3COOH) to create CH_4, CO and CO_2. Besides, the nickel addition could prevent the aggregation of Cu species, and thus it was able to facilitate the dispersion of Cu^{2+} ions on the catalyst surface. As a result, the ethanol conversion was improved significantly, thereby marginally increasing hydrogen production.

Jo et al. [22] aimed to enhance the quantity of hydrogen produced and long term catalytic stability of Ni-based core@shell catalysts during the steam reforming of ethanol by introducing certain amounts of Mn. These authors synthesized five different core@shell $30Ni_xMn_y@70SiO_2$ using co-precipitation and impregnation methods. At reaction temperature of 700^{o}C, the hydrogen selectivity obtained over catalysts with Mn/Ni molar ratio greater than 0.05 was noticeably high, especially in the case of $30Ni_{8.5}Mn_{1.5}@70SiO_2$ catalyst, at 94% after 8 hours, and those great performances were sustained over a period of 10 hours. Of the investigated samples, the one without Mn addition ($30Ni@70SiO_2$) exhibited poor activity in terms of both hydrogen production and ethanol conversion. This catalyst presented hydrogen selectivity of around 75% after 3 hours, but this value rapidly decreased towards the end of the reaction period, at only 50% after 10 hours. For ethanol conversion, it took this sample up to 5 hours to convert more than 90% of inlet ethanol into products, whereas the others needed just 2 hours to achieve that. When it comes to product distribution, all catalysts produced H_2, CH_4, CO and CO_2 as the main products, but the methane selectivity declined tremendously as increasing

the amount of Mn doped. Additionally, the CO_2 selectivity over $30Ni_xMn_y@70SiO_2$ samples was much higher than that over the nickel-only counterpart. This finding, according to the authors, could be explained by the fact that methane steam reforming and water gas shift (WGS) reactions were favored over $30Ni_xMn_y@70SiO_2$ catalysts. Another important factor affecting the catalytic activity was the coke formation on the catalyst surface. The samples with Mn introduction had much lower amounts of coke deposition, except for $30Ni_{8.0}Mn_{2.0}@70SiO_2$. The spent $30Ni_{8.5}Mn_{1.5}@70SiO_2$ had the lowest quantity of deposited carbon coke, the deposited carbon chains of which were short, suggesting that the extent of catalytic deterioration caused by coke formation was likely reduced. The improvement in coke-resistance of $30Ni_xMn_y@70SiO_2$ catalysts probably resulted from their better reactant adsorption capacity. Indeed, Ni sites accommodated CH_4 and CO gases, while water molecules were adsorbed more easily on Mn species. CO, the precursor of carbon lumps that covered active sites of the catalysts, was turned into CO_2 through WGS reaction with water, contributing to the decline in catalytic deactivation. To sum up, the introduction of Mn brought about positive effects on the catalytic activity of Ni-based core@shell catalysts owing to the capability of Mn to promote the adsorption of water, which was the crucial reactant in steam reforming and WGS reactions.

Divins et al. [13] examined the effect of nano-architectured CeO_x in $RhPd/CeO_2$ for ethanol steam reforming reaction and realized that the hydrogen yields attained over catalysts with ceria nanocubes and nanorods was higher than that over the catalyst with polycrystalline ceria in the range of 650-750K. However, this difference diminished at temperatures higher than 800K. The factors behind the improved activity of $RhPd/CeO_2$-cubes and $RhPd/CeO_2$-rods for ESR at low temperature primarily stemmed from the occurrence of metal organization on (100) and (110) crystallographic planes, which were the predominant facets enclosed in ceria nanocubes and nanorods, respectively. The structure of RhPd alloy and its interaction with the support affected the WGS reaction. Moreover, the nature of support influenced the extent of reducibility, oxygen transport and prevalence of

undercoordinated sites, which also directly related to the WGS performance. In order to understand more clearly the advantages of ceria nanocubes and nanorods, the authors explained that the capacity for oxygen vacancies significantly relied on morphology. The energy necessary for producing oxygen vacancies on the (111) plane of CeO_2 was higher than those on (110) and (100) planes, meaning that the amount of oxygen vacancies corresponding to each plane varied considerably. Specifically, the quantity of energy required for oxygen vacancies production on the (111) plane would be highest, followed by the (110) plane, and lastly the (100) plane. This indicated that (100) and (110) planes were able to create higher amounts of oxygen vacancies to encourage the catalytic ESR reaction. Polycrystalline ceria nanoparticles had mainly (111) planes to reduce surface energy, while the predominantly exposed planes of CeO_2 nanorods were (110) and (100) planes and the (100) plane in the case of nanocubes.

Soykal et al. [19] delved into the effect of ceria morphology (nanorods ── NR, and nanocubes ── NC) on the Co/CeO_2 catalysts for ethanol steam reforming in the 350 – 500^{o}C range with H_2O/EtOH molar ratio of 10 and recounted that CeO_2 nanocubes exposed mostly the (110) plane, and that Co catalysts supported on nanocubes were more reducible than those supported on nanorods or commercial supports of similar particle size. In addition, H_2 and CO_2 were favored products on those catalysts in the 400 - 500^{o}C range, while Co/CeO_2 (NR) had limited capability to break the C-C bond and therefore the dominant product created was acetaldehyde. There were some reasons for this difference in catalytic performance. Firstly, from XRD analysis, the authors found that the relative intensity of the (220) plane for ceria nanocubes was remarkably higher than that for ceria nanorods (71% and 52%, respectively). The (110) plane could create more oxygen vacancies, which play an pivotal role in promoting the movement of oxygen atoms in the lattice, the dissociation of water molecules and the diffusion rate of oxygen, resulting in the improved catalytic performance in ESR. In addition, the anionic vacancies that compose surface defects could help to stabilize the metal oxide species during the impregnation process, and thanks to this metallic dispersion was boosted

significantly. Apart from the support, the relative intensity of the peak corresponding to Co_3O_4 for Co/CeO_2-NR was 18%, compared to only 5% for Co/CeO_2-NC. This indicated that the catalyst based on ceria nanorods had larger particle size for cobalt oxide on the surface, leading to lower metal dispersion after reduction. Secondly, the dispersion of metallic cobalt with Co/CeO_2-NC was 21%, which was three times higher than that with Co/CeO_2-NR, at 7%. The cause of this dissimilarity might be either better reduction of cobalt oxide in Co/CeO_2-NC or larger Co particles on the nanorods, as mentioned in the XRD analysis. Moreover, the cubes possessed a higher proportion of the smaller pores (20–40 Å range), and those small pores could prevent cobalt species from aggregating during the impregnation since it was proved that Co expressed a strong preference for small diameter pores on the Co/CeO_2-NC sample.

Moraes et al. [20] researched the effect of ceria morphology on catalytic performance of Ni/CeO_2 catalysts for low temperature steam reforming of ethanol (temperature of 300 – 400°C, H_2O/EtOH molar ratio of 3). These researchers revealed that Ni supported on CeO_2 nanostructures (nanocubes: CeO_2-NC, nanorods: CeO_2-NC and flower-like: CeO_2-FL) facilitated the ethanol decomposition reaction at low temperature in comparison with Ni supported on conventional polycrystalline ceria obtained from the precipitation method (CeO_2-PPT). The XRD results were adduced to explain this finding. The Ni crystallite size calculated by XRD for Ni/CeO_2-PPT was larger than those for other catalysts, and larger particle size may be responsible for lower metal surface, on which the decomposition reaction took place. H_2-TPR results showed that ceria reducibility as well as NiO reduction were not affected by ceria morphology. At 300°C, all catalysts gave the same product distribution with H_2, CO_2, acetaldehyde, CO and CH_4 being the main products. The catalyst deactivation occurred rapidly over those catalysts, implying the formation of nickel carbide phase and the presence adsorbed acetate species. Regarding coke formation, the Ni/CeO_2-NC sample was found to have the largest amount of carbon, whereas the one supported on the rods exhibited the lowest carbon deposition. As reaction temperature was raised to 400°C, ethanol conversion reached a peak at 100% and

remained stable throughout a period of 28 hours. Also, acetaldehyde was no longer detected in the effluent, and CO selectivity decreased along with the increase in the amount of CO_2 created, suggesting that ethanol decomposition and WGS reaction were promoted under such condition. Increasing reaction temperature also produced higher quantity of coke due to the Boudard reaction ($2CO \rightarrow C + CO_2$), which was favored at high temperature.

CHAPTER 3: EXPERIMENTAL

3.1. Chemicals

All chemicals used in this research are listed in Table 4 below.

Table 4: Chemicals and their sources

Chemicals	Sources
Nickel(II) nitrate hexahydrate $Ni(NO_3)_2.6H_2O$	Merck
Manganese(II) nitrate tetrahydrate $Mn(NO_3)_2.4H_2O$	Merck
Copper(II) nitrate trihydrate $Cu(NO_3)_2.3H_2O$	Ajax
Cerium(III) nitrate hexahydrate $Ce(NO_3)_3.6H_2O$	Merck
Ethanol absolute 99.9%	QRëC
Helium gas 99.999%	Praxair
Hydrogen gas 99.99%	Praxair
Standard mixture gas 1% of H_2, 1% CO, 1% CO_2, 1% CH_4, 1% C_2H_4, 1% C_2H_6 with balance N_2	BOC scientific

3.2. Instruments for Catalyst Preparation

All instruments used for catalyst preparation are shown in Table 5 below.

Table 5: Instruments used and their origins

Instruments	Model	Company
Magnetic stirrer	C-MAG HS7	IKA®
Drying oven	100-800	MEMMERT GmbH + Co.
4 - decimal place balance	AB204-S	METTLER TOLEDO
Lab furnace	ELF 11/14B	CARBOLITE GERO
50ml and 250ml beakers		PYREX®
Stainless steel vessel		
Teflon-lined cylinder		

3.3. Instruments for Ethanol Steam Reforming

- Quartz tube reactor
- Mass flow controller
- Gas chromatography (Shimadzu GC-2014) for gaseous products
- Gas chromatography (Shimadzu GC – 14B) for liquid product
- Flow meter (Agilent Technologies)
- Syringe pump
- Evaporator
- Thermocouple
- Condenser
- Tube furnace and temperature controller

3.4. Catalyst Preparation

CeO_2 support was prepared via precipitation method (CeO_2-P). Aqueous solutions with appropriate amounts of $Ce(NO_3)_3.6H_2O$ and NaOH were used as the precursor of ceria and the precipitator, respectively. The mixture solution was heated to 90^0C under stirring condition at 600 rpm and maintained for 5 hours. The pH value of the mixture was kept constant at 10. Subsequently, the suspension was filtered to get the desired precipitate having yellowish color. The resulting solid was then thoroughly washed with deionized water and dried at 110°C overnight, followed by calcination at 600°C for 4 hours in air.

Ceria nanocubes (CeO_2-NC) and CeO_2 nanorods (CeO_2-NR) were synthesized by means of the hydrothermal method mentioned in previous literature [18, 23]. To obtain CeO_2-NC, two separate solutions were first prepared. The solution of NaOH (solution I) consisted of 7.2g NaOH dissolved in 30ml distilled water, whereas the solution II contained 6.4g $Ce(NO_3)_3.6H_2O$ and 36ml distilled water. The next step would be combining these two solutions together to create a milky suspension, followed by vigorous stirring for 30 minutes. After that, the mixture was transferred to a Teflon-lined cylinder and tightly sealed in a stainless steel autoclave, which was then put into an oven already preheated to 180°C and kept for 25 hours. Following this, the autoclave was cooled naturally to room temperature, and the precipitate was recovered using suction filtration. The collected product was carefully washed with deionized water to remove unwanted ions and with ethanol to prevent nanoparticles from agglomerating. Finally, the solid was dried at 110°C overnight and calcined under air atmosphere at 450°C for 4 hours.

For CeO_2-NR, the preparation stages were similar to those of CeO_2-NC, except for the hydrothermal treatment temperature, which was constantly kept at 100°C to ensure the formation of the desired nanorods morphology.

In the first phase, Ni-Mn/CeO_2-P catalysts were synthesized by incipient wetness co – impregnation of the ceria support with aqueous solutions of $Ni(NO_3)_2.6H_2O$ and $Mn(NO_3)_2.4H_2O$ to obtain 12% metals by weight. The loading of Mn

were varied, started with 0%wt in the 100Ni sample and increased to 10%, 20%, 30% and 50% in the samples of 10Mn90Ni, 20Mn80Ni, 30Mn70Ni and 50Mn50Ni, respectively. Accordingly, the loading of Ni were balanced correspondingly to the Mn loading in order to preserve the total metal loading of 12% as introduced before. After co – impregnation step, the as – prepared catalysts were dried at 110°C overnight and calcined at 450°C for 3 hours in air.

The similar procedure was applied in the case of Ni-Cu/CeO_2-P series to prepare 4 more samples, namely 10Cu90Ni, 20Cu80Ni, 30Cu70Ni and 50Cu50Ni. However, it would be a bit different for the Ni-Cu-Mn/CeO_2-P series, where the total metal loading was still 12%, but the proportion of Ni was maintained constantly at 6%. The other 6% was allocated to both Cu and Mn. As a result, 5 samples were synthesized and denoted as Ni10Cu90Mn, Ni30Cu70Mn, Ni50Cu50Mn, Ni70Cu30Mn, and Ni90Cu10Mn.

In the second phase, the metal loading with the best activity would be supported on CeO_2-NR and CeO_2-NC and compared with that on CeO_2-P. The experiments would be based on a full 2^4 factorial design, and after screening four factors to identify any significant effects upon hydrogen yield, a FCCCD-RSM (face-centered central composite-response surface methodology) with three independent screened factors would be employed to find out the optimum conditions so as to obtain maximal hydrogen yield. All details of the 2^4 factorial design, FCCCD-RSM and the validation of the model were provided in section 3.6.

3.5. Catalyst Characterization

3.5.1. X-Ray Diffraction (XRD)

The X – Ray powder diffraction (XRD) patterns of the catalysts were gathered by Bruker D8 Advance X – ray Powder Diffractometer using CuKα radiation (λ = 1.5406 Å).

3.5.2. Temperature Programmed Reduction (TPR)

TPR experiments were conducted by a Micromeritics AutoChem II 2920 fully automated chemisorption analyzer. The samples were first pretreated under Ar flow rate of 40cm^3/min at 500°C for 1 hour with the heating rate of 10°C/min. After this pretreatment step, the catalysts were cooled to the room temperature. Next, the reducing mixture (10 vol% of H_2 in Ar) was introduced to the reactor at a flow rate of 40cm^3/min and the temperature was raised to 700°C with a heating rate of 10°C/min.

3.5.3. X-Ray Fluorescence (XRF)

The chemical composition of each sample in Ni-Mn/CeO_2-P series was measured by Wavelength Dispersive X-Ray Fluorescence Spectrometer (WD-XRF), Bruker model S8 Tiger. The quantitation method used theoretical formulas (fundamental parameter calculations). The measurement method was Best Detection-He8mm.

3.5.4. Nitrogen adsorption/desorption

BET surface areas were measured by nitrogen adsorption/desorption using a Micromeritics ASAP 2020 V4.00 analyzer.

3.5.5. Thermogravimetric Analysis (TGA)

The mass loss measurements were carried out in a TGA Q50 V6.7 Build 203 instrument. Around 10 mg of used catalyst was heated under oxygen atmosphere from 200°C to 900°C with a heating rate of 10°C/min to determine the change in weight.

3.5.6. Transmission Electron Microscopy (TEM)

TEM and HRTEM images were collected from JEM-2100 from JEOL, Japan.

3.6. Catalytic tests

The ethanol steam reaction was evaluated in a quartz – tube packed – bed reactor (Figure 4) at atmospheric pressure. Deionized water and absolute ethanol were mixed together in suitable proportions to create desired steam to ethanol (S/E) molar ratios. The samples were placed between layers of quartz wool and then put in the middle of the reactor. The flow rate of the liquid mixture was kept unchanged at 1 mL/h, while the amounts of catalysts were adjusted to give the weight of catalyst to ethanol flow rate (W/F_{EtOH}) ratio corresponding to each specific experiment. The flow of carrier, helium, purity 99.999%, was controlled at 40 mL/min to assure stable liquid evaporation. Prior to reaction, the catalysts were reduced in hydrogen (40 vol% H_2/He, 80 mL/min) at 400°C for 1.5 hours and then purged under helium at the same temperature for 30 minutes to remove excessive hydrogen on the surface of catalysts. The ethanol aqueous solution was fed into the evaporator operating at 150°C by a syringe pump and diluted with helium before being introduced to the reactor. All the lines from the evaporator to the reactor and from the reactor to the condenser were heated to 150°C using heating tapes to prevent condensable components from condensing somewhere along the whole system.

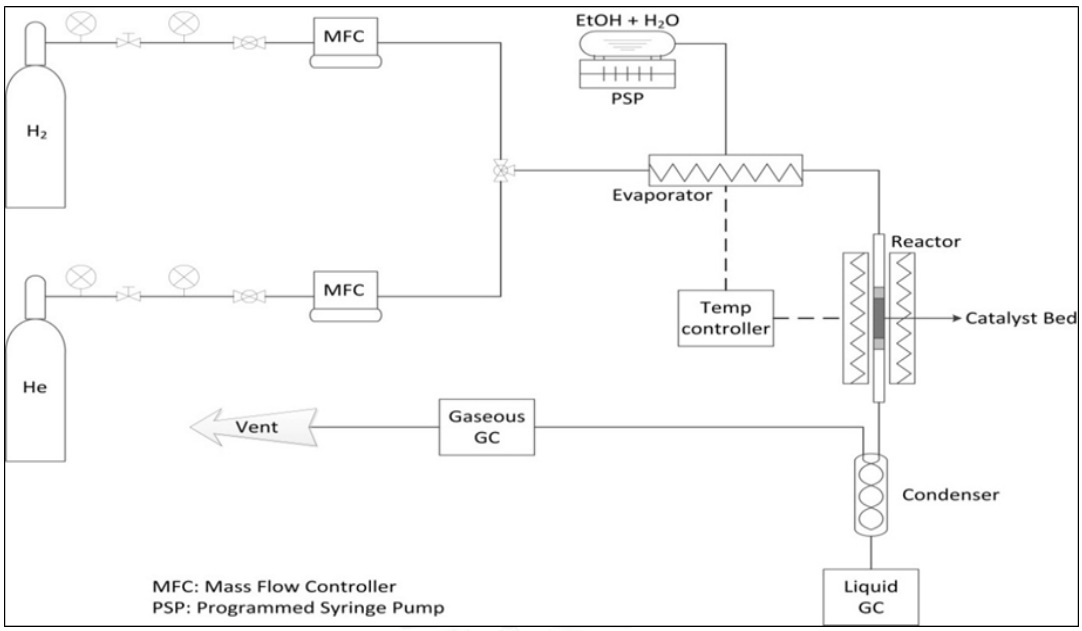

Figure 4: Schematic diagram of experimental set – up

The effluent gaseous products were analyzed on-line using a Shimadzu GC 2014 gas chromatography with Shincarbon column via TCD detector, whereas the liquid products collected in the condenser (C_2H_5OH, CH_3CHO, and CH_3COCH_3) were determined off - line by a Shimadzu GC – 14B equipped with DB Wax column and FID detector. The reaction time was 2 hours for all experiments. A Universal Gas Flow-meter model ADM1000 (Agilent Technologies) was used to measure the flow rate of the dry outlet stream. Outlet molar flow rates of non-condensable products (CO, CH_4, and CO_2) could be calculated based on the combination of the total volumetric flow rate of the effluent gaseous products and the analyzed composition from the GC. All the catalysts in the first phase were undergone the ESR process under fixed conditions presented in Table 6 below.

Table 6: Reaction parameters for the first phase of the research

Reaction parameter	Value
Temperature	400°C
S/E ratio	3
Weight of catalyst to ethanol flow rate (W/F_{EtOH})	22.44g_c

In the second phase, a matrix of full 2^4 factorial design experiments with four central points would be constructed and conducted to further examine the catalytic performance of the best metal loading found in the previous phase. The investigated factors were temperature, ceria morphology, S/E ratio and W/F ratio. The ethanol conversion and hydrogen yield were used as the responses for statistical analysis. All experiments were conducted in a randomized order to minimize random errors and were repeated two times to obtain averaged results. A software package, Design Expert 7.0 (Stat Ease Inc. Minneapolis, USA), was utilized to analyze the data gained from experiments. From this software, a normal probability plot, response surface plots, an ANOVA (analysis of variance) table with a Pareto chart of absolute standardized effect at P-value = 0.05 were subsequently created to assess the significance and the influence of each factor on the responses. A student's test with a corresponding P-value would be used, and any factors possessing P-value lower than 0.05 would be regarded as significant variables. The detailed experimental matrix of the full 2^4 factorial design including four central points is shown in Table 7, where -1, 0, and +1 represent the low level, the central point and the high level, respectively, on the real scale of each factor. The levels of factor B-Ceria morphology were based on the BET surface areas of three ceria morphologies. Specifically, the morphology with the lowest surface area (nanocubes-37.4 m^2/g) was encoded as -1, whereas conventional polycrystalline ceria (BET surface area of 53.6 m^2/g) and ceria nanorods (BET surface area of 71.6 m^2/g) were encoded as 0 and +1, respectively.

After carefully evaluating the important effects based on the factorial design, a FCCCD-RSM (face-centered central composite-response surface methodology) was applied in search of the optimum conditions for hydrogen yield (see Table 8). The levels of chosen factors remained unchanged. In order to check the correctness of the model, 4 additional experiments based on the examined factors were carried out, and the results derived from those experiments were compared with estimated values.

Table 7: The experimental matrix of the full 2^4 factorial design

Factors	Variables	Unit	Low level	Center	High level
A	Temperature	^{o}C	400	500	600
B	Ceria morphology	-	Nanocubes	Polycrystalline	Nanorods
C	S/E ratio	-	3	5	7
D	W/F ratio	$g_{cat}h/mole_{EtOH}$	7.48	14.96	22.44
Standard order	Run order	A	B	C	D
1	13	-1	-1	-1	-1
2	14	1	-1	-1	-1
3	5	-1	1	-1	-1
4	6	1	1	-1	-1
5	11	-1	-1	1	-1
6	12	1	-1	1	-1
7	3	-1	1	1	-1
8	4	1	1	1	-1
9	15	-1	-1	-1	1
10	16	1	-1	-1	1
11	7	-1	1	-1	1
12	8	1	1	-1	1
13	9	-1	-1	1	1
14	10	1	-1	1	1
15	1	-1	1	1	1
16	2	1	1	1	1
17	17	0	0	0	0
18	18	0	0	0	0
19	19	0	0	0	0
20	20	0	0	0	0

Table 8: The design matrix for FCCCD-RSM

Standard order	Run order	A	B	C
1	7	-1	-1	-1
2	8	1	-1	-1
3	3	-1	1	-1
4	4	1	1	-1
5	5	-1	-1	1
6	6	1	-1	1
7	1	-1	1	1
8	2	1	1	1
9	17	-1	0	0
10	9	1	0	0
11	11	0	-1	0
12	10	0	1	0
13	16	0	0	-1
14	15	0	0	1
15	12	0	0	0
16	13	0	0	0
17	14	0	0	0

3.7. Catalytic performance evaluation

The catalytic activity of catalysts was assessed through ethanol conversion (X_{EtOH}), hydrogen yield (Y_{H_2}) and the selectivity towards the carbon-containing products ($S_{CO}, S_{CO_2}, S_{CH_4}, S_{C_2H_4}, S_{C_2H_6}, S_{CH_3CHO}$ and $S_{CH_3COCH_3}$) as follows (Eqs. (5) - (13)):

$$X_{EtOH} = \frac{\left(moles_{EtOH,in} - moles_{EtOH,out}\right)}{moles_{EtOH,in}} \times 100 \quad (5)$$

$$Y_{H_2}[\%] = \frac{moles_{H_2},out}{6\left(moles_{EtOH,in}\right)} \times 100 \quad (6)$$

$$S_{CO}[\%] = \frac{moles_{CO}/2}{\left(moles_{EtOH,in} - moles_{EtOH,out}\right)} \times 100 \quad (7)$$

$$S_{CH_4}[\%] = \frac{moles_{CH_4}/2}{\left(moles_{EtOH,in} - moles_{EtOH,out}\right)} \times 100 \quad (8)$$

$$S_{CO_2}[\%] = \frac{moles_{CO_2}/2}{\left(moles_{EtOH,in} - moles_{EtOH,out}\right)} \times 100 \quad (9)$$

$$S_{C_2H_4}[\%] = \frac{moles_{C_2H_4}}{\left(moles_{EtOH,in} - moles_{EtOH,out}\right)} \times 100 \quad (10)$$

$$S_{C_2H_6}[\%] = \frac{moles_{C_2H_6}}{\left(moles_{EtOH,in} - moles_{EtOH,out}\right)} \times 100 \quad (11)$$

$$S_{CH_3CHO}[\%] = \frac{moles_{CH_3CHO}}{\left(moles_{EtOH,in} - moles_{EtOH,out}\right)} \times 100 \quad (12)$$

$$S_{CH_3COCH_3}[\%] = \frac{moles_{CH_3COCH_3}/\left(2/3\right)}{\left(moles_{EtOH,in} - moles_{EtOH,out}\right)} \times 100 \quad (13)$$

3.8. Operating condition of the GC

Table 9 shows the condition required to assure the GC to operate effectively with the aim of detecting and quantitatively assessing every single gas in the gaseous outlet stream.

Table 9: Operating condition of the Shimadzu GC 2014 gas chromatography

Carrier gas	Helium, purity 99.999%		
Column type	Shincarbon		
Injector temperature	100°C		
	Rate (°C/min)	Temperature (°C)	Hold time (min)
Column temperature program	-	50.0	1.00
	10.00	70.0	0.00
	20.00	250.0	0.00
Detector temperature	120°C		
Detector type	Thermal conduct detector (TCD)		

CHAPTER 4: RESULTS AND DISCUSSIONS

4.1. Characterization

4.1.1.Structural Analysis of Catalysts

The X – ray diffraction (XRD) patterns of calcined Ni – Mn/CeO_2-P samples are shown in Figure 5 where the predominant peaks were found at about 28.5°, 33°, 47.5°, and 56.4° (2θ) corresponding to the (111), (200), (220), and (311) planes of cubic structure of CeO_2 (JCPDS 34-0394), respectively, with the most intense and sharp diffraction line appearing at 2θ = 28.5° from the (111) plane. In addition, peaks having weak relative intensities occurred at 2θ values of around 37.4°, 43.2°, and 62.8° representing (111), (200), and (220) crystalline faces of NiO phase (JCPDS 44-1159). The intensities of these peaks, however, decreased with the increase of the amount of Mn doped in the nickel – based catalysts and completely vanished in the case of 50Mn50Ni, suggesting that either the dispersion of NiO was facilitated by the presence of manganese oxides or the amount of these species was too low to be detected by XRD. Another point to be considered is that there was not any peak of manganese oxides, indicating the integration of entire manganese ions into the ceria lattice. This finding is highly consistent with those recounted by other researchers [17, 24].

Bampenrat et al. [17] supposed that the dissolution of Mn in the ceria lattice might happen as the ionic radii of Mn^{4+} (5.6 nm) and Mn^{3+} (6.2 nm) were smaller than that of Ce^{4+} (9.7 nm). In order to strengthen the assumption mentioned above, the diffraction peaks of Ni – Mn/CeO_2 catalysts equivalent to the (111) plane were zoomed in and expressed in Figure 6. As can be seen from this figure, these peaks slightly shifted to higher values as the content of Mn rose, which proved the unification of Mn cations into the ceria lattice.

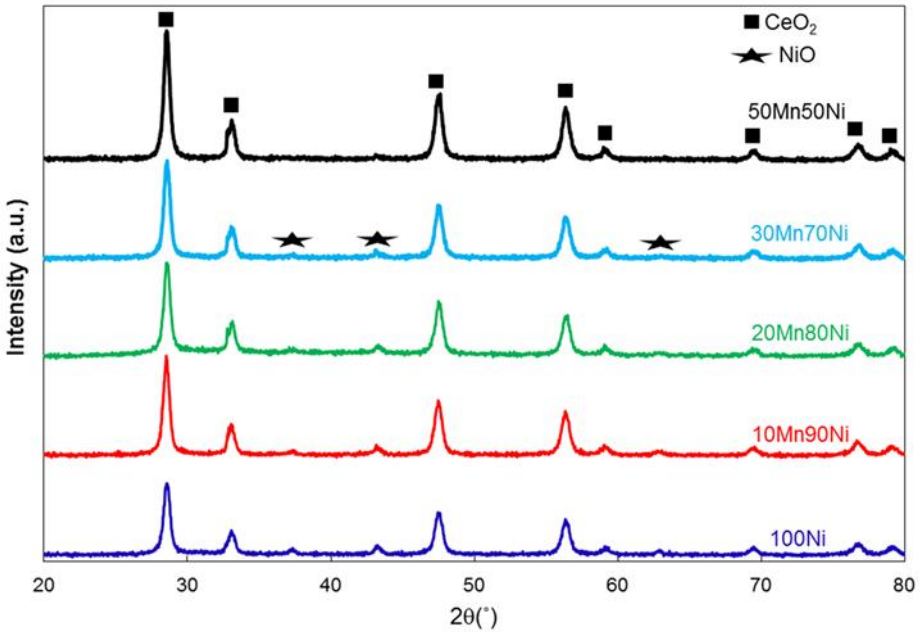

Figure 5: XRD patterns of Ni-Mn/CeO_2-P catalysts

Figure 7 illustrates the diffractograms of Ni-Cu/CeO_2-P catalysts. Apart from the same peaks representing cubic structure of CeO_2 and NiO phase as those of Ni-Mn series mentioned above, one can easily recognize two reflections at 2θ = 35.6° and 2θ = 38.8°, designated as the (002) and (111) planes, respectively, of CuO monoclinic crystal phase [25], in the spectrum of the 50Cu50Ni sample. This implies that Cu species did not enter into the ceria lattice but aggregated to form larger crystals that could be identified by XRD. Furthermore, NiO species were likely to strongly interact with CeO_2 since there was not any obstacle between them. As a result, reduction temperatures of this series were higher than those of the Ni-Mn counterparts (as shown in the next TPR section) due to low dispersion of the CuO crystallites and the stronger interaction between NiO species and the support.

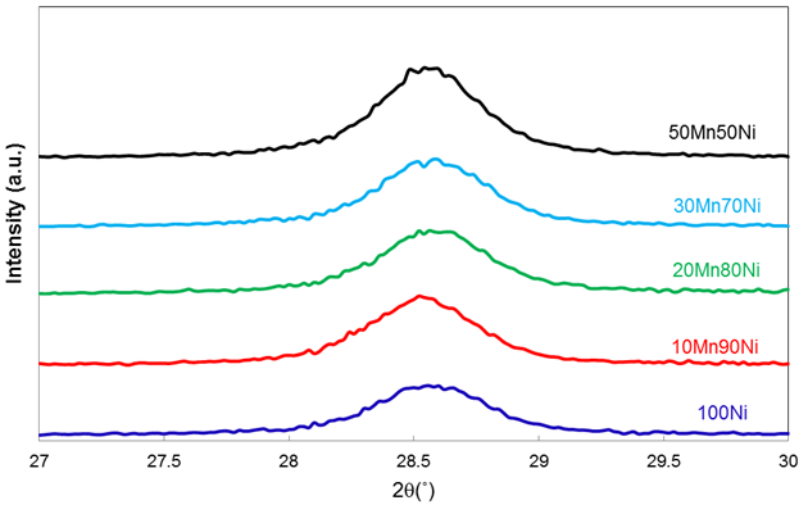

Figure 6: The enlarged image of (111) plane of CeO_2 of Ni – Mn/CeO_2-P catalysts

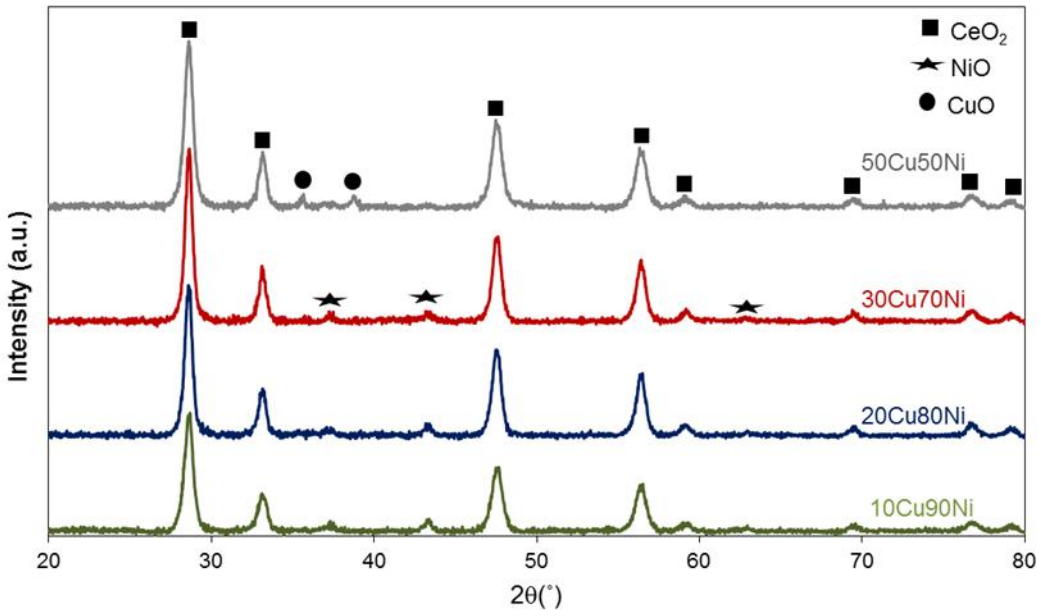

Figure 7: XRD patterns of Ni-Cu/CeO_2-P catalysts

In the case of Ni-Cu-Mn series (Figure 8), all the peaks related to NiO totally disappeared in all spectra, whereas the diffraction line of the Ni90Cu10Mn catalyst still revealed the reflections of CuO. The XRD once again could not detect any diffraction peak of Mn species.

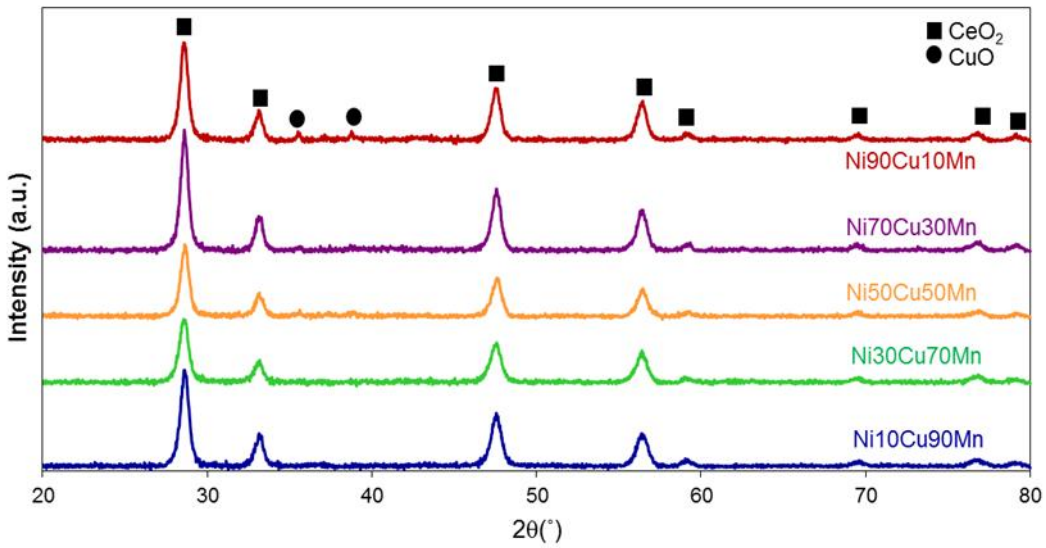

Figure 8: XRD patterns of Ni-Cu-Mn/CeO_2-P catalysts

The XRD patterns of catalysts for the second phase are shown in Figure 9, where 10Mn90Ni-P, 10Mn90Ni-NR and 10Mn90Ni-NC were the catalysts supported on conventional polycrystalline ceria, ceria nanorods and ceria nanocubes, respectively. It is notable that the diffraction lines of catalysts supported on CeO_2 nanorods and nanocubes were more intense, implying that the grain sizes of CeO_2 nanorods and nanocubes were higher than those of the sample with conventional polycrystalline ceria. Moreover, the peaks corresponding to the (220) plane of ceria slightly moved to higher values of 2θ as the morphology of the support varied from polycrystalline to nanorods and nanocubes, which could be interpreted in the sense that 10Mn90Ni-NR and 10Mn90Ni-NC would have more oxygen vacancies than 10Mn90Ni-P (Figure 10) [26]. Table 10 below presents crystallite sizes of CeO_2 and NiO calculated by Scherrer equation as well as the position of ceria (220) peaks (2θ).

Table 10: Crystallite sizes of CeO_2 and NiO calculated by Scherrer equation and position of ceria (220) peak (2θ)

Sample	d (nm)		Position of ceria (220) peak (2θ)
	CeO_2[a]	NiO[b]	
10Mn90Ni/CeO_2-P	16	27	47.46°
10Mn90Ni/CeO_2-NR	21	14	47.52°
10Mn90Ni/CeO_2-NC	60	14	47.48°

[a] calculated by using the (111) ceria plane

[b] calculated by using the (200) NiO plane

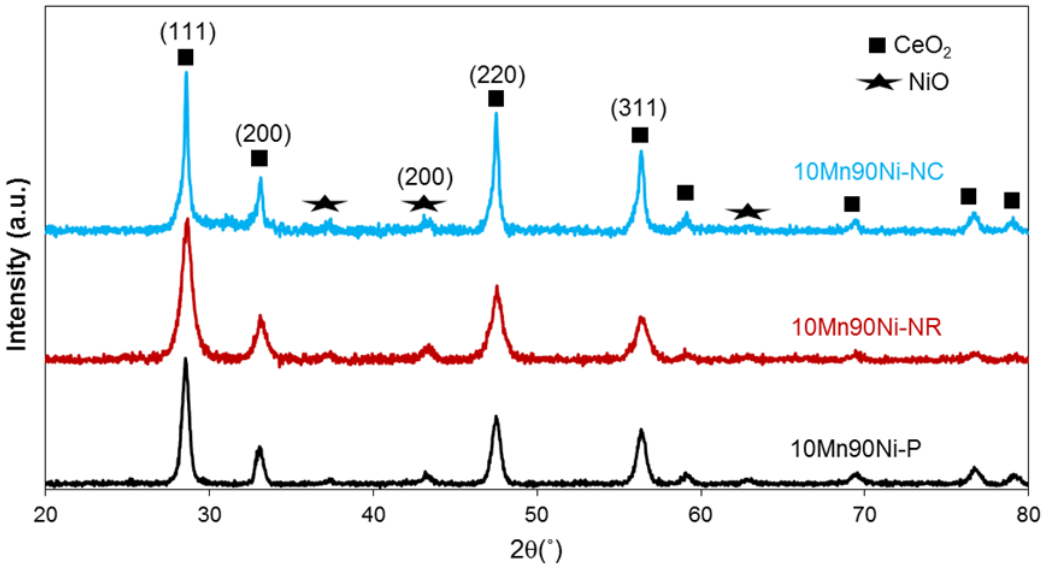

Figure 9: XRD patterns of 10Mn90Ni/CeO_2 catalysts with different supports

Another interesting result worth noticing is that the intensity of the peak related to the ceria (220) plane of the sample 10Mn90Ni-NC was incredibly high. When the intensity of the ceria (111) plane of each sample was considered the standard level, the intensity of the (220) plane of ceria nanocubes was equal to 76%

of that of the standard, whereas the equivalent figures for ceria nanorods and polycrystalline ceria were only 53% and 52%, respectively. As mentioned in the literature review, the density of oxygen vacancies of the (110) family planes ((220) in this case) is significantly high, thereby partly promoting the ESR process [18, 19, 26].

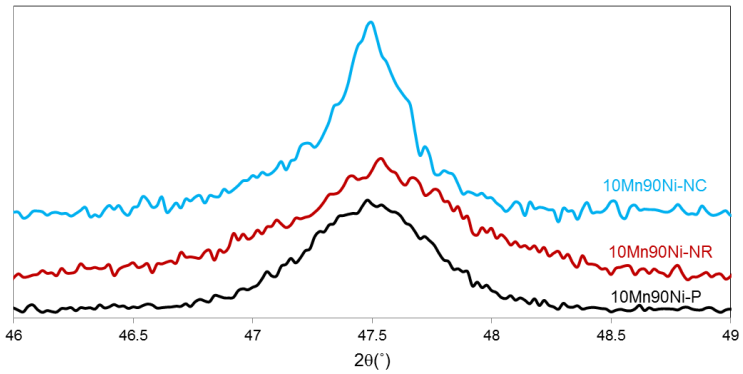

Figure 10: The enlarged image of (220) plane of ceria of 10Mn90Ni/CeO_2 catalysts with different morphologies of the support.

4.1.2. Reduction Behavior Analysis of Catalysts

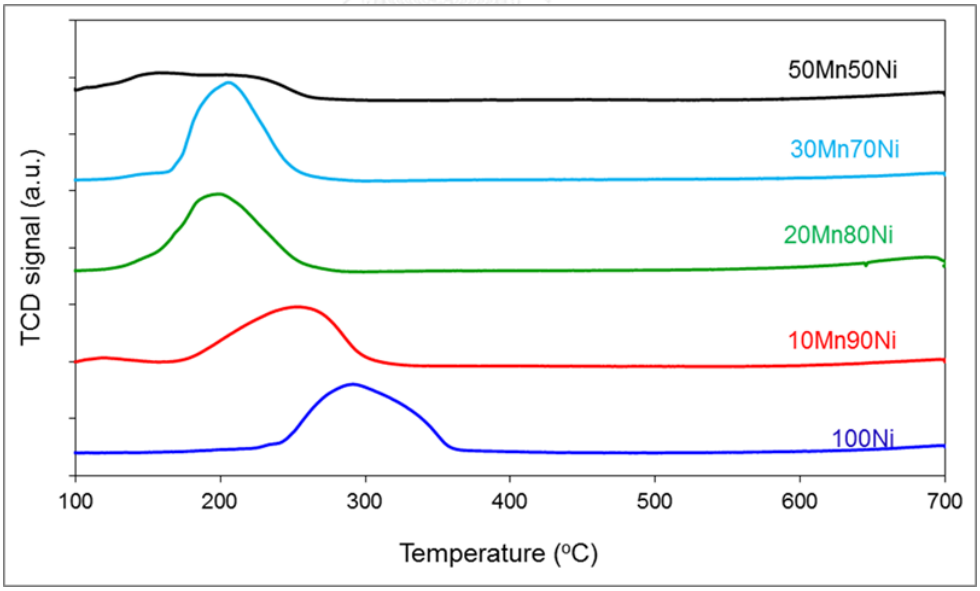

Figure 11: TPR profiles of Ni – Mn/CeO_2-P catalysts

Figure 11 shows the TPR profiles of Ni – Mn/CeO_2-P catalysts. It is clear that all samples exhibit only one reduction peak in the range of 200 – 300°C although those are bimetallic catalysts (except for the 100Ni sample), and this peak

can be attributed to the reduction of NiO [23]. In addition, the temperature of the peak apparently shifted to lower values as increasing the concentration of Mn. This indicates that the incorporation of Mn into the ceria lattice mentioned in the XRD part prevented NiO species from strongly interacting with the support by infiltrating into the lattice of ceria and therefore facilitated the dispersion of NiO on the CeO_2 surface. Thus, the reducibility of active phase was improved considerably. Also, this could help to generate higher oxygen mobility, which means that more mobile oxygen was produced during the reforming process.

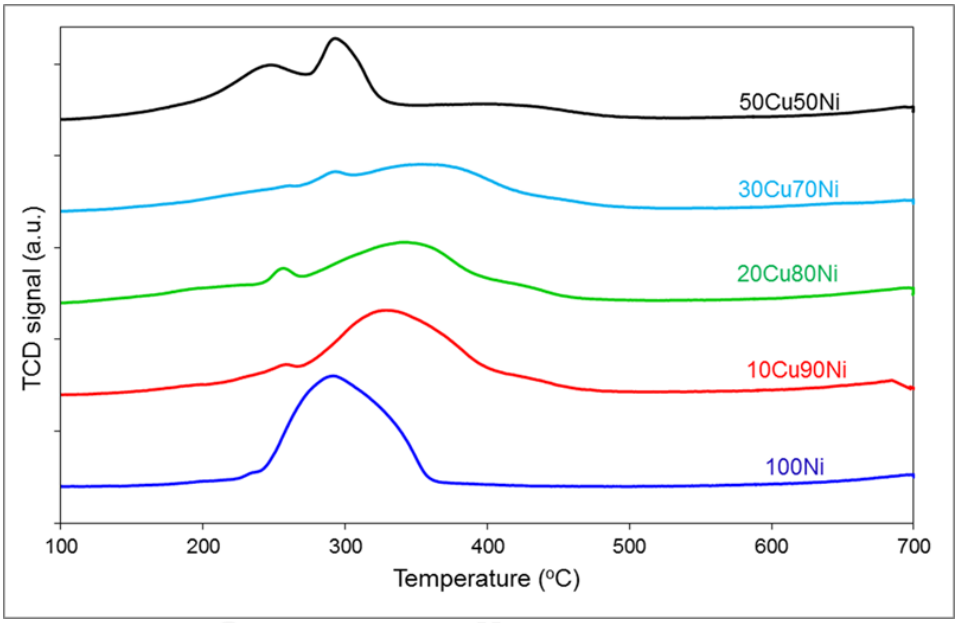

Figure 12: TPR profiles of Ni – Cu/CeO_2-P catalysts

TPR patterns of Ni-Cu/CeO_2-P display 2 peaks at 250 – 285 and 320 – 360°C (Figure 12). The first peak can be reasonably ascribed to the reduction of CuO, and hydrogen consumption equivalent to the second one is possibly corresponding to the reduction of NiO species [27]. The intensities and reduction temperatures of these peaks generally moved to higher values with the increase of Cu content, except the 50Cu50Ni sample. This is probably because Cu species could not hinder the NiO from entering the ceria lattice, as opposed to Mn in Ni-Mn/ CeO_2-P series. Moreover, the interaction between NiO and CuO could make the catalysts less reducible, which is similar to the results of Chen et al [9]. Those authors found that

increasing the molar ratio of Cu/Ni in Cu-Ni/SiO_2 catalysts would favor the Cu-Ni alloy structure formation and slightly shift the reduction temperatures to higher values.

Figure 13 presents results from TPR measurements of Ni – Cu - Mn/CeO_2-P catalysts. Overall, there was only one H_2 consumption peak for all trimetallic catalysts being investigated in the range of 145-205°C, which is much lower than that of the nickel-only sample, at 291°C. The finding in this section is in good agreement with those obtained from Ni-Cu and Ni-Mn series explained above, where the rise in the content of Cu brought about a detrimental effect on the reducibility of the catalysts, whilst the opposite trend could be witnessed in the case of Mn doping.

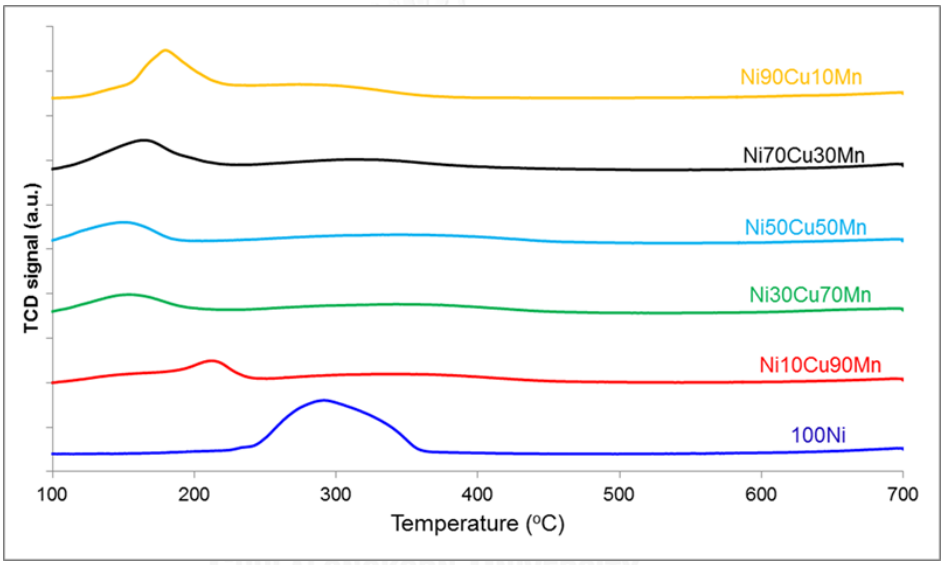

Figure 13: TPR profiles of Ni – Cu - Mn/CeO_2-P catalysts

The TPR profiles of catalysts for the second phase are displayed in Figure 14. The profiles of samples with ceria nanocubes (10Mn90Ni-NC) and bulk ceria (10Mn90Ni-P) showed only one H_2 uptake peak at 320°C and 253°C, respectively, corresponding to the reduction of NiO as discussed above. The higher reduction temperature of the sample with ceria nanocubes might result from the larger crystallite sizes of both ceria and NiO species, as mentioned in the XRD section. By contrast, the curve of the catalyst with ceria nanorods (10Mn90Ni-NR) was divided into 3 separate peaks, the first one of which at 265°C may be due to the decomposition residual nickel nitrates [23]. The other peaks at 304°C and 365°C,

according the literature [22], could involve the reduction of NiO and Ni_6MnO_8 to metallic Ni, respectively, although the XRD failed to detect the presence of this spinel. This is largely because the XRD peaks of Ni_6MnO_8 overlapped those of NiO at low dopant concentration [22].

From the TPR outcomes above, it is reasonable to predict that catalysts with ceria nanocubes and nanorods would be active at temperatures higher than 400°C since at those temperatures all NiO and/or Ni-containing compounds would be completely reduced to the corresponding metal.

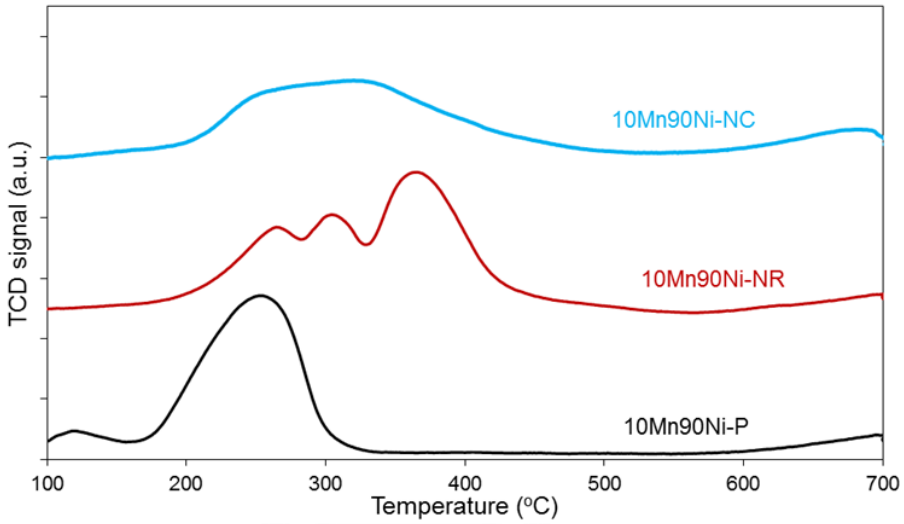

Figure 14: TPR profiles of 10Mn90Ni/CeO_2 catalysts with different supports

4.1.3. Physical Properties of Ni-Mn/CeO_2-P Catalysts

Since both XRD and TPR failed to recognize the presence of Mn species in this series, XRF analysis was utilized. In addition to that, textural properties of each sample was also added (see Table 11).

The XRF results expressed that all samples were acceptable because the actual values measured from XRF were close to the calculated nominal values, confirming the existence of Mn in those catalysts. Regarding the results gained from BET surface analyzer, the BET surface areas and total pore volumes of all samples slightly decline with the increasing Mn amount, except the 30Mn70Ni and 50Mn50Ni catalysts. This exception could be ascribed to the formation of two different types of

particles from ceria and manganese oxides, which has been explained before by Blanco et al. [28]. Large particles (>50 nm) of cerium - free Mn oxides may dominate the 10Mn90Ni and 20Mn80Ni samples, whereas the 30Mn70Ni and 50Mn50Ni samples observed a significant contribution to the surface of small crystals (<7 nm) of a Ce – Mn solid solution, thereby resulting in higher surface area. Moreover, the average pore diameters are in the range of 5.7 – 6.2 nm which is in good agreement with that discovered by Bampenrat et al. [17].

Table 11: Physical properties of Ni-Mn/CeO_2-P catalysts

Sample	Chemical composition (wt%)[a]						Surface area (m^2/g)[b]	Total pore volume (cm^3/g)[b]	Average pore diameter (nm)[b]
	Nominal			Real					
	CeO_2	Mn	Ni	CeO_2	Mn	Ni			
100Ni	85.2	0.0	12.0	85.9	0.0	11.4	25.4	0.038	6.1
10Mn90Ni	84.9	1.2	10.8	84.1	1.1	11.1	20.8	0.032	6.1
20Mn80Ni	84.6	2.4	9.6	84.8	2.0	9.5	18.7	0.029	6.2
30Mn70Ni	84.3	3.6	8.4	85.0	2.8	8.3	22.0	0.034	6.2
50Mn50Ni	83.7	6.0	6.0	84.1	5.0	6.2	25.2	0.036	5.7

[a] Determined by XRF

[b] Determined by BET surface analyzer

4.1.4. BET Surface Area

BET surface areas, pore volumes and average pore diameters of the three supports and Ni – Mn/CeO_2 catalysts are listed in Table 12. Overall, ceria nanorods had by far the highest surface area and total pore volume, which were almost twice as high as those of the cubes. The second highest figures came to bulk ceria. Average pore diameters of the supports followed the same pattern, but the extent of disparity among them was not too considerable.

Table 12: Textural properties of all supports and 10Mn90Ni/CeO_2 catalysts

Sample	Surface area (m^2/g)	Total pore volume (cm^3/g)	Average pore diameter (nm)
CeO_2-P	53.6	0.096	7.2
CeO_2-NR	71.6	0.132	7.4
CeO_2-NC	37.4	0.053	5.7
10Mn90Ni-P	20.8	0.032	6.1
10Mn90Ni-NR	41.9	0.071	6.8
10Mn90Ni-NC	38.5	0.053	5.5

After impregnation, the surface area, pore volume and pore diameter of ceria nanorods and conventional polycrystalline ceria declined significantly, whereas equivalent values of ceria nanocubes appeared to remain almost unchanged. The similar result could be found in the work of Moraes et al. [29] who studied the activity of PtNi/CeO_2-nanocubes catalysts for ethanol steam reforming. According to these authors, ceria with cubic shapes derived from hydrothermal method possessed a surface area of 31m^2/g, and this figure increased to 35m^2/g and 36 m^2/g when being impregnated with nickel and nickel plus platinum, respectively. Therefore, it could be concluded that this type of support was not considerably influenced by the addition of nickel.

4.1.5. Transmission Electron Microscopy (TEM)

Three markedly different morphologies of ceria could be clearly seen from the TEM analysis (Figure 15). The hydrothermal treatment at 100^{o}C and 180^{o}C using a concentrated NaOH solution for a long reaction time (25 hours) resulted in the formation of ceria nanorods and nanocubes, respectively. This finding has been reported by Mai et al. [30], who proposed the shape-selective mechanism for forming CeO_2 nanorods and nanocubes. Specifically, when mixing solutions containing Ce^{3+}

ions and NaOH, anisotropic $Ce(OH)_3$ nuclei were produced immediately. Next, high-base environment ($C_{NaOH} = 6M$ for this work) and prolonged reaction time (25 hours) at the hydrothermal temperature of $100^{\circ}C$ fostered the rate of dissolution/recrystallization to urge the $Ce(OH)_3$ nuclei to develop anisotropically into pure CeO_2 nanorods, which demonstrated 1D structure that grew preferably along the [110] crystallographic direction with enclosing (110) and (100) planes. As the temperature went up to $180^{\circ}C$, the conversion of $Ce(OH)_3$ to CeO_2 nanocubes enclosed by (100) facets was favored due to the instability and oxidation of those nuclei.

Figure 15(a) depicts ceria nanocubes with particle sizes of 10-15nm, whereas nanorods counterparts (Figure 15(b)) exhibited average widths and lengths of 4-8nm and 30-50nm, respectively. Ceria prepared by precipitation method exposed predominantly (111) planes with sizes ranging from 8nm to 20nm (Figure 15 (c))

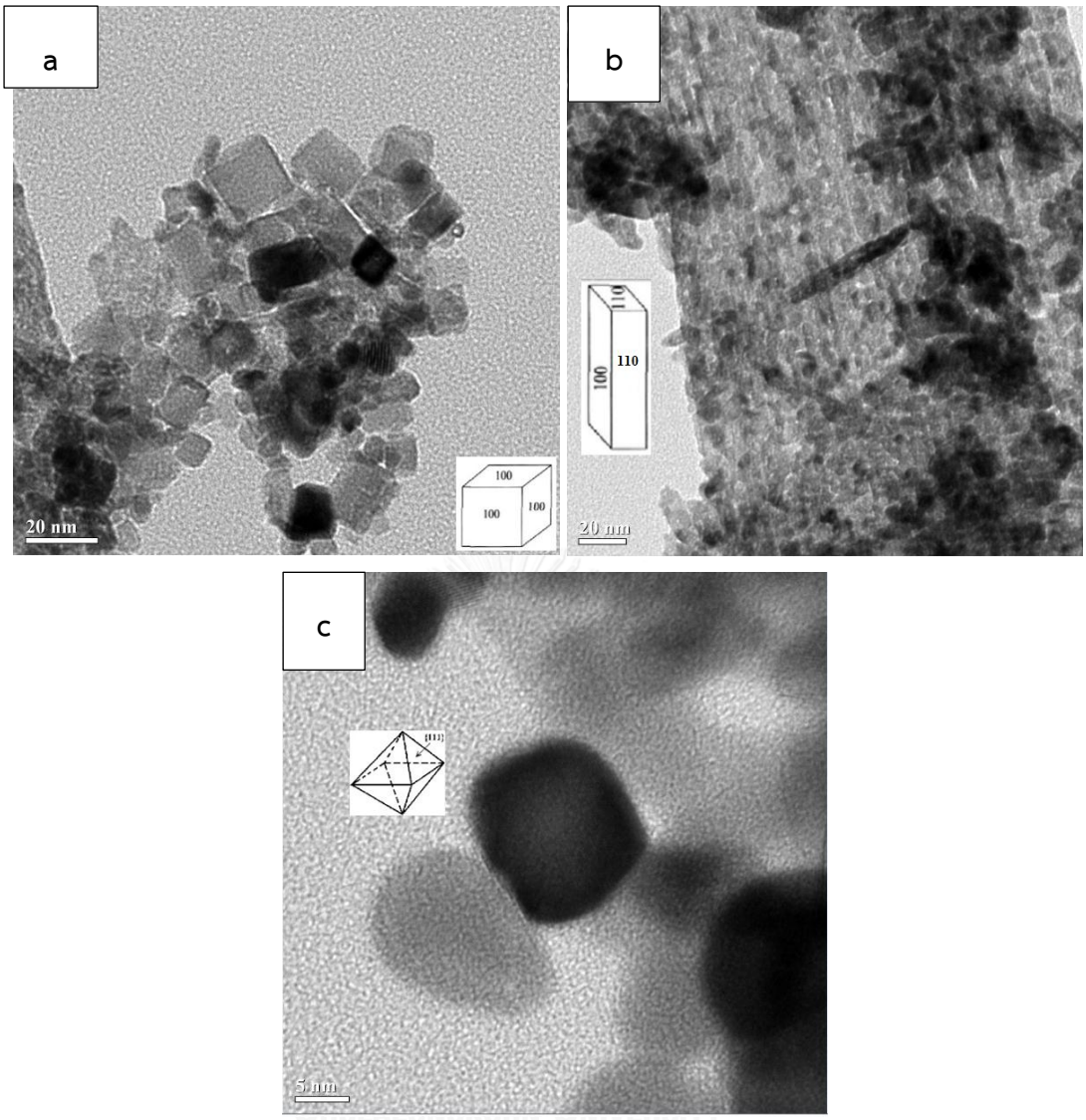

Figure 15: TEM images for 3 ceria morphologies: (a) ceria nanocubes, (b) ceria nanorods, (c) conventional polycrystalline ceria.

4.2. Catalytic Performance

4.2.1. The results for the phase "Identifying"

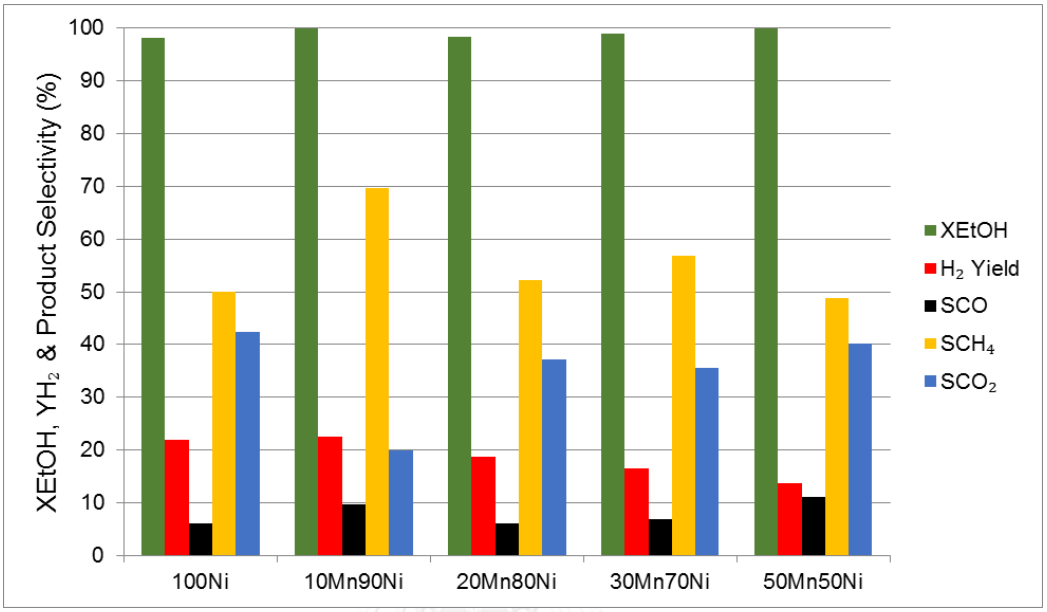

Figure 16: Ethanol conversion (X_{EtOH}), hydrogen yield (Y_{H_2}) and product selectivity over the Ni-Mn/CeO_2-P catalysts at 400°C, S/E = 3, W/FEtOH = 22.4gcath/moleethanol.

Ethanol conversion, hydrogen yield and product selectivity obtained over the Ni – Mn/CeO_2-P catalysts with different metal loadings are depicted in Figure 16. It is easily recognizable that all catalysts exhibited nearly 100% ethanol conversion at the tested conditions, of which the 10Mn90Ni and 50Mn50Ni samples showed total conversion and the others were able to convert more than 98% alcohol into products. In addition, the hydrogen yield attained was slightly bolstered when adding 10% Mn to the nickel catalyst, but further doping this promoter brought about a detrimental effect on the amount of hydrogen generated from the reforming. The CH_4 selectivity shared the same tendency with the hydrogen production, which reached a peak of around 70% for the sample of 10Mn90Ni and then witnessed a downward trend over the remaining samples.

On the other hand, there was an opposite trend in the CO_2 selectivity that started at more than 40% over the Ni – only catalyst, and next dropped dramatically to 20% over 10Mn90Ni before gradually increasing to 40% again over 50Mn50Ni. Besides, the selectivity toward CO was significantly low, less than 10% for all the catalysts.

Another interesting point can be observed from the product distribution is that the popular intermediate of the process, acetaldehyde, was not detected in the effluent.

Combined with the facts illustrated above, it is conceivable to conclude that the decomposition of ethanol ($CH_3CH_2OH \rightarrow CH_4 + H_2 + CO$) and water – gas shift ($CO + H_2O \leftrightarrow CO_2 + H_2$) reactions were favored. The improved performance of Mn – promoted catalysts could be attributed to the better oxygen mobility and reducibility of active phase resulted from the incorporation of Mn into ceria lattice, as discussed in the XRD analysis and H_2-TPR sections. Nevertheless, excessive addition of Mn along with the subtraction of Ni possibly led to the fall in hydrogen yield since it would reduce the amount of active phase in steam reforming of ethanol.

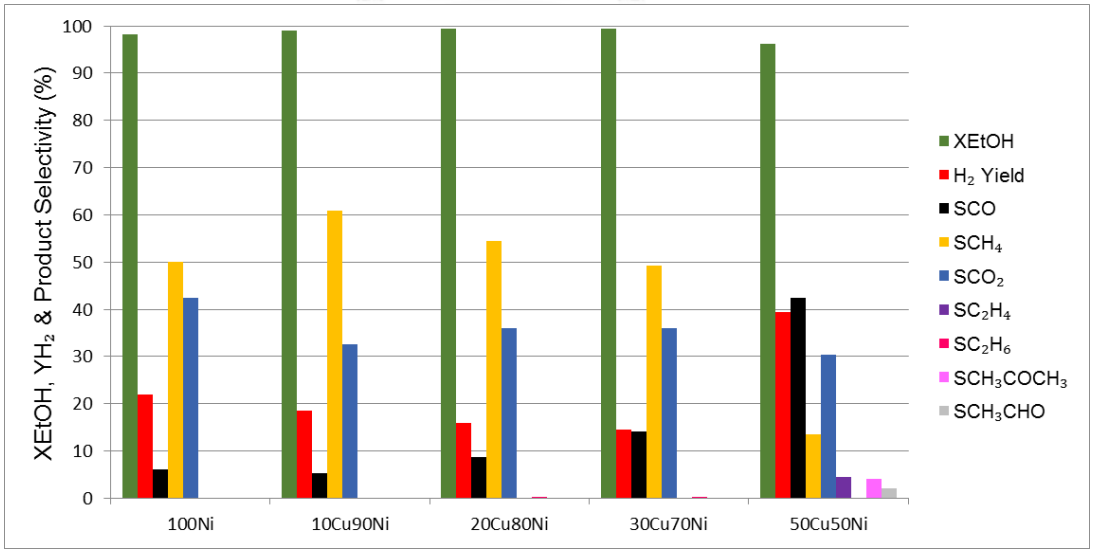

Figure 17: Ethanol conversion, hydrogen yield and product selectivity over the Ni-Cu/CeO_2-P catalysts at 400°C, S/E = 3, W/F_{EtOH} = 22.4$g_{cat}h/mole_{ethanol}$.

Figure 17 shows the catalytic activity of Ni-Cu/CeO_2-P catalysts. As can be seen from the chart, the catalysts demonstrated similar activity to that derived from the Ni – Mn series, except the 50Cu50Ni sample with the presence of acetaldehyde and acetone.

The amount of hydrogen production experienced a moderate fall of more than 18% to 14.54% over 10Cu90Ni and 30Cu70Ni respectively and subsequently showed an enormous jump to around 40% over 50Cu50Ni. CH_4 was the product that had highest selectivity, at around 60% over the first sample but gradually dropped as the loading of copper went up to 30%, whereas the figure for CO was only 5% at the beginning and then slightly increased over the next two catalysts.

The percentage of CH_4 saw a significant decrease to approximately 14% over 50Cu50Ni. By contrast, the proportion of CO rose dramatically to roughly 42% over the same sample and became the highest fraction of the products selectivity. Moreover, the rate for CO_2 fluctuated insignificantly but in general remained steady in the range of 30% to 36%.

Apart from the gaseous products mentioned above, the most striking difference between this series and Ni – Mn catalysts came from small quantities of intermediates and ethylene which occurred over 50Cu50Ni. This indicated a weaker C – C bond breaking activity and higher tendency towards dehydration compared to samples with lower copper content.

When trimetallic catalysts were utilized, the product distribution changed dramatically with CO being the most dominant component among carbon-containing gases (Figure 18). In detail, a great majority (more than 40%) of inlet carbon from ethanol turned into CO over every sample, whereas the overall figures for CO_2 and CH_4 were less than 30% and 20%, respectively. In addition, the ethanol conversion slightly declined, accompanied by the rise of acetone and acetaldehyde formation as larger amounts of copper were added into the catalysts. Those catalysts, however, created comparable hydrogen production to that from bimetallic Ni-Cu counterparts,

except for Ni50Cu50Mn and Ni90Cu10Mn which exhibited better hydrogen yield than other samples, at around 30% and 21% respectively.

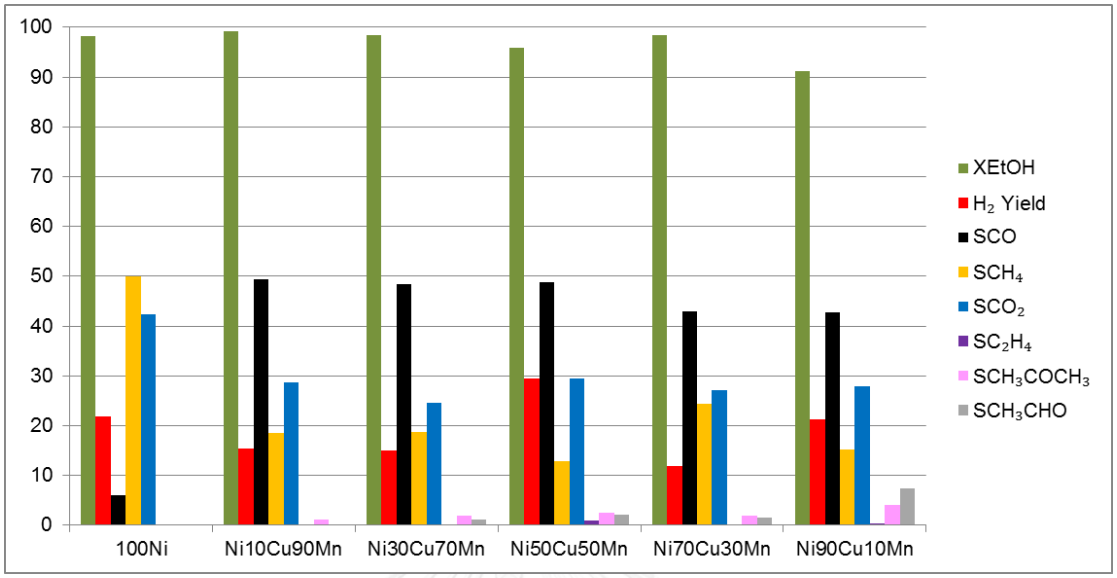

Figure 18: Ethanol conversion, hydrogen yield and product selectivity over the Ni-Cu-Mn/CeO_2-P catalysts at 400°C, S/E = 3, W/F_{EtOH} = 22.4$g_{cat}h/mole_{ethanol}$.

After carefully evaluating the product distributions of three series of catalysts, it is conceivable to suppose that the samples with high Cu content favored two reaction pathways. The first one is that ethanol molecules were transformed to acetaldehyde through dehydrogenation, and acetaldehyde species then underwent decomposition to form CH_4 and CO. In the second pathway, dehydration reaction would convert an ethanol molecule into ethylene, and the formed ethylene was subsequently reformed to CO and H_2 by steam reforming reaction or directly to coke. This explains the remarkable amounts of H_2 generated over those catalysts. On the other hand, the strong tendency to CO, a poison for the PEM fuel cells, should be taken into account to reduce the cost of purification steps after the reforming stage. Therefore, the sample of 10Mn90Ni would be chosen for further examination in the second phase of the research since it gave total ethanol conversion, relatively high H_2 yield and low concentrations of undesired products.

4.2.2. The results for the phase “Measuring”

To determine the significance of four independent factors on the ethanol conversion and hydrogen yield, a matrix of full 2^4 factorial design experiments with four central points was constructed. All experiments were conducted with replication, and the data listed in the Table 13 below represented the mean value of each run (the specific data of the two repetitions was presented in the Appendix).

Ethanol conversion as the response

There is an interesting point worth attention here is that all the experiments gave almost total ethanol conversion (≥ 98%). In other words, the catalysts were able to transform close to or entire inlet alcohol into products under investigated conditions regardless of ceria morphology, W/F ratio and temperature. The similar results have been reported by Moraes et al. [23] for steam reforming of ethanol over Ni/CeO_2 catalysts. In this case, the ethanol conversion and product distribution were independent of the ceria shape, and the temperature to achieve total conversion was 400°C. Therefore, this response would not be further analyzed. Instead, the hydrogen yield would be carefully studied.

Table 13: Experimental variables in coded and actual unit for a full 24 factorial design with four central points

Factors		Variables		Unit		Low	Medium	High
A		Temperature		^{o}C		400	500	600
B		Ceria morphology		-		Nanocubes	Poly-crystalline	Nanorods
C		S/E ratio		-		3	5	7
D		W/F ratio		g_{cat}h/moleEtO		7.48	14.96	22.44
Standard order	Run order	A	B	C	D	Ethanol conversion (%)		Hydrogen yield (%)
1	13	-1	-1	-1	-1	98.2		9.6
2	14	1	-1	-1	-1	97.8		28.8
3	5	-1	1	-1	-1	98		17.2
4	6	1	1	-1	-1	98.2		33.4
5	11	-1	-1	1	-1	100		14.7
6	12	1	-1	1	-1	100		38.1
7	3	-1	1	1	-1	100		24.2
8	4	1	1	1	-1	100		40.5
9	15	-1	-1	-1	1	98.6		11.1
10	16	1	-1	-1	1	98.9		30
11	7	-1	1	-1	1	99.1		13.2
12	8	1	1	-1	1	98		28.9
13	9	-1	-1	1	1	98.9		16.8
14	10	1	-1	1	1	98.9		37.9
15	1	-1	1	1	1	100		23.6
16	2	1	1	1	1	100		43.1
17	17	0	0	0	0	98		28.2
18	18	0	0	0	0	98		29.2
19	19	0	0	0	0	98		29.6
20	20	0	0	0	0	98		31.7

Hydrogen yield as the response

The hydrogen yield as the response was first evaluated by means of statistical analysis with the normal probability plot of the effect estimates (Figure 19). This figure was compartmentalized into two regions; the region with normal % probability higher than 50% contained positive effects and interactions, while negative counterparts were situated in the region below 50%. It is clearly seen that the effect of temperature (A), Morphology (B) and S/E ratio (C) lay far away from the red line, whereas the remaining effects and interactions were distributed along the same line, indicating that A, B and C had a profound impact on hydrogen yield outcomes. This assessment is reinforced by the Pareto chart showing the absolute standardized effect at a 95% confidence interval (Figure 20). Only the effects of A, B and C possessed the absolute values higher than the Bonferroni limit (3.48), and this could act as a suggestion that those factors significantly affected the hydrogen yield.

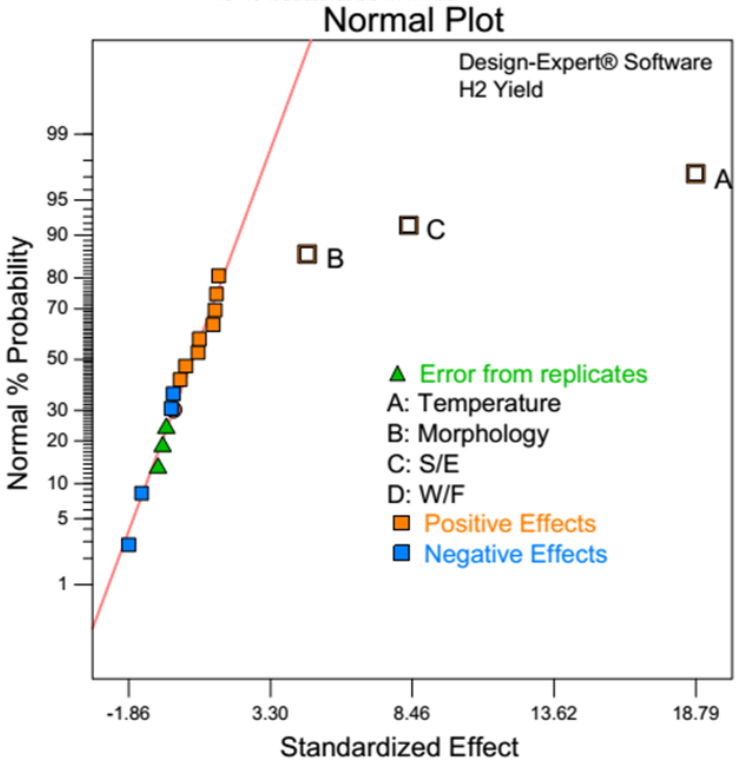

Figure 19: Normal probability plot of the effects for the 2^4 factorial design

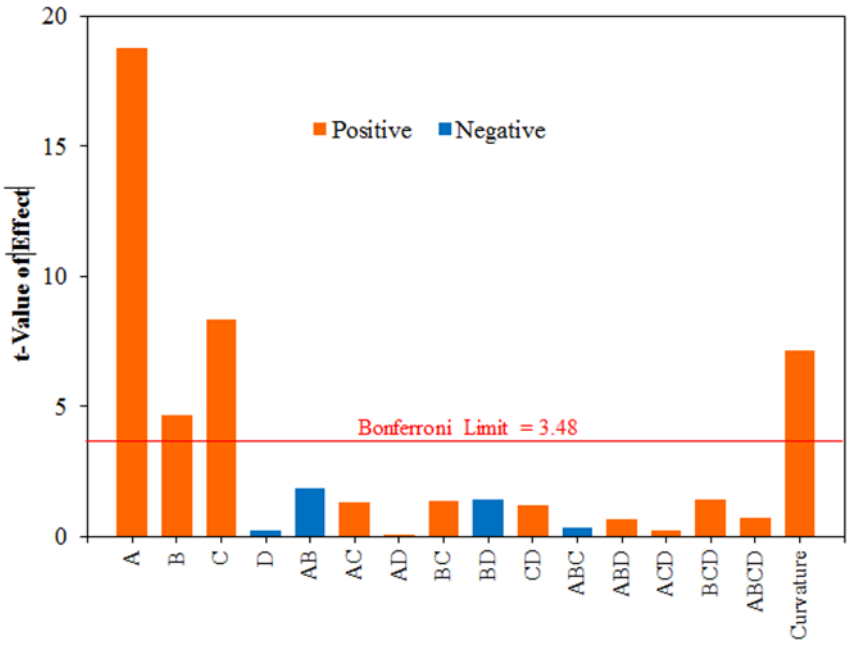

Figure 20: The Pareto chart of the factors for the 2^4 factorial design

Table 14: Analysis of Variance for the Hydrogen Yield Response in A, B and C

Source	Sum of Squares	DF	Mean square	F value	P-value	Contribution (%)
Model	1775.96	3	591.99	147.22	< 0.0001	
A	1411.88	1	1411.88	351.13	< 0.0001	74.82
B	86.03	1	86.03	21.39	0.0003	4.56
C	278.06	1	278.06	69.15	< 0.0001	14.74
Curvature	50.72	1	50.72	12.61	0.0029	2.69
Residual	60.31	15	4.02			3.19
Cor total	1887	19				
R-Squared	0.9672					
Adj R-Squared	0.9606					

Table 14 summarizes the analysis of variance for the hydrogen yield response from the full 2^4 factorial design in terms of 3 main effects, namely A, B and C, at a 95% confidence interval. It is clear that the P-values of A – temperature, B – ceria morphology and C – S/E ratios were all lower than 0.05, implying the statistical significance of those effects on the hydrogen yield. Besides, the percentage contribution to the total sum of squares again consolidated the influence of the three factors. Looking at the percentage contribution in more detail, the main effect of temperature (A) had highest contribution, with 74.82%, followed by that from S/E ratio, with 14.74%. By contrast, the figure for ceria morphology was only 4.56%. The "curvature F-value" of 12.61 signified that there was significant curvature (as measured by difference between the average of the center points and the average of the factorial points) in the design space. There was only a 0.29% chance that a "Curvature F-value" this large could occur due to noise. The R^2 and adjusted R^2 values of the regression model were quite high, at 0.9672 and 0.9606 respectively, indicating a strong similarity between predicted values and those derived from experiments. The regression equation (in terms of coded factors) of the H_2 yield ($\mathbf{Y}_{H_2}$) could be expressed as follows:

$$\mathbf{Y}_{H_2}(\%) = 25.69 + 9.39\mathrm{A} + 2.32\mathrm{B} + 4.17\mathrm{C}$$

Figure 21(a) illustrates the effect of temperatures and different steam to ethanol molar ratios on the H_2 yield with CeO_2 nanorods as the catalyst support and an unchanged W/F ratio of 7.48g_{cat}h/mole EtOH. Overall, higher levels of reaction temperature and S/E ratio would bring about a greater amount of H_2 generated from the reforming process and vice versa. At any predetermined proportion of S/E molar ratio, a rise in temperature created the linear growth in H_2 production. Such trend could be explained by the fact that the steam reforming reactions of methane ($CH_4 + H_2O \longrightarrow CO + 3H_2$; $CH_4 + 2H_2O \longrightarrow CO_2 + 4H_2$) and acetaldehyde ($C_2H_4O + H_2O \longrightarrow 3H_2 + 2CO$; $C_2H_4O + 3H_2O \longrightarrow 5H_2 + 2CO_2$) were thermodynamically facilitated at high temperatures.

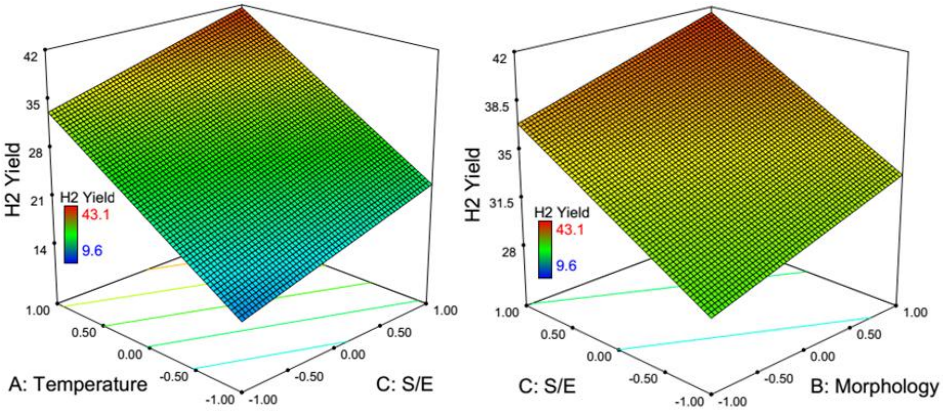

Figure 21: H_2 yield response surface plots of (a) A and C effects with CeO_2 nanorods and W/F ratio of 7.48 g_{cat}h/mole EtOH and (b) B and C effects with temperature of 600°C and W/F ratio of 22.44 g_{cat}h/mole EtOH

However, if the content of CO, a toxic gas, in the product stream is taken into account, then the reforming temperature should not be kept at too high values since the water gas shift (WGS) equilibrium would shift backward, creating a remarkable unconverted CO amount [2, 3, 11]. That is why the examined temperatures in this research were maintained in the range of 400°C to 600°C. According to the figure, the H_2 yield rose almost 2 times, from 22.8% to 41.6%, as the temperature went up from 400°C to 600°C respectively with S/E ratio being kept constant at 7. The comparable tendency could be realized when looking at the CO selectivity response surface plot (Figure 22). At 400°C, S/E ratio of 7, W/F ratio of 7.48g_{cat}h/mole EtOH, and CeO_2 nanorods as the support, while only 8.0% of carbon in the influent ethanol turned into CO, this figure soared up to 50.71% as increasing temperature to 600°C and maintaining the remaining effects unchanged.

Similarly, excessive amount of H_2O in the feed stream was favorable for a large quantity of H_2 derived from the reforming reactions. Several authors have also mentioned to this finding before, specifically stating that water plays a remarkable role in the reforming process by driving the WGS equilibrium forward and enhancing the methane consumption through the steam reforming of this gas, as well as inhibiting the formation of undesired intermediates such as acetaldehyde and ethylene [3, 4, 10-13]. As a result, more H_2 and CO_2 would be produced along with

the decrease in CO and CH_4 selectivity. Looking more closely at the effect of S/E ratio, there was a relatively sharp climb from 33.2% to 41.6% when increasing the S/E ratio from 3 to 7 with temperature being controlled at 600^{o}C using ceria nanorods as the support. Too much water in the inlet stream, on the other hand, could make the operating costs drastically higher because of the corresponding amount of heat for vaporizing the liquid mixture of ethanol and water [9, 14]. In addition, H_2O molecules may compete with other reactants to adsorb on the catalyst surface during the reaction process, and this blockage effect reduces the number of available active sites on which the reactions take place. Therefore, suitable S/E ratio must be carefully considered to satisfy both economic and performance requirements.

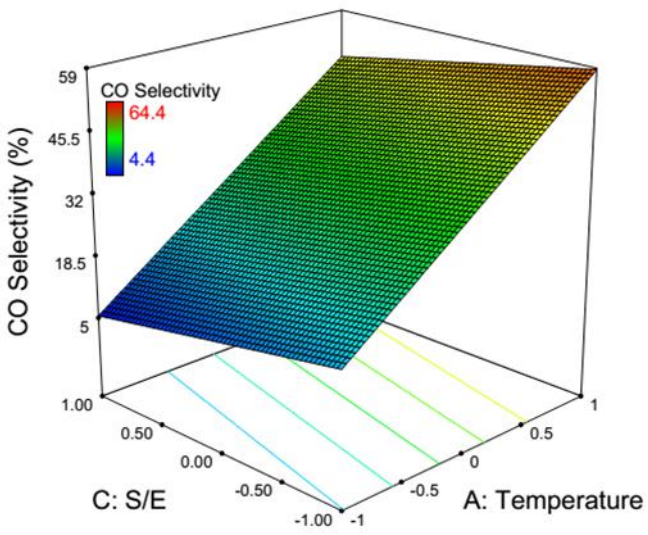

Figure 22: CO selectivity response surface plot of A and B effects with CeO_2 nanorods and W/F ratio of 7.48 g_{cat}h/mole EtOH

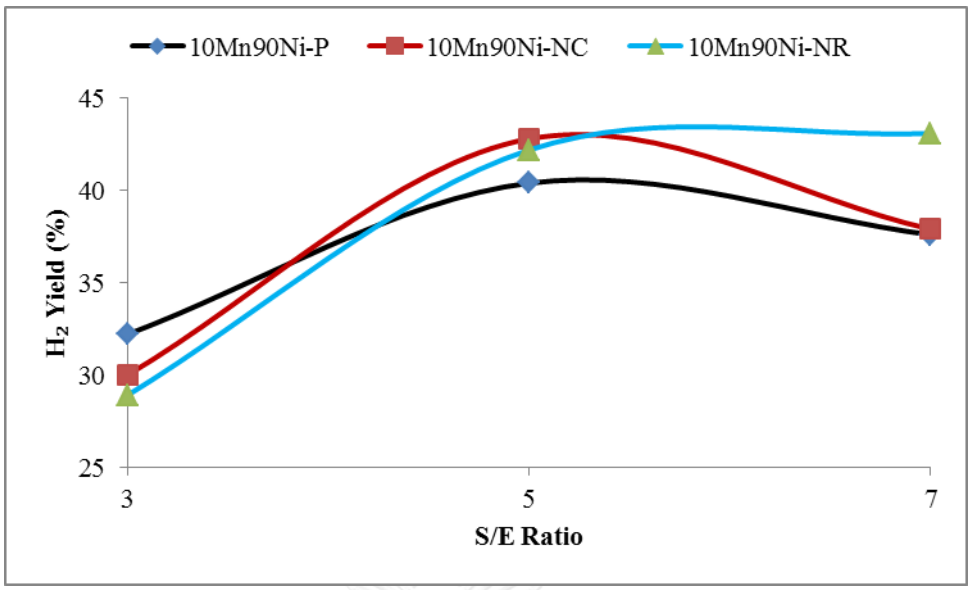

Figure 23: H_2 yields with respect to S/E ratios of 10Mn90Ni catalysts supported on different ceria morphologies at 600°C

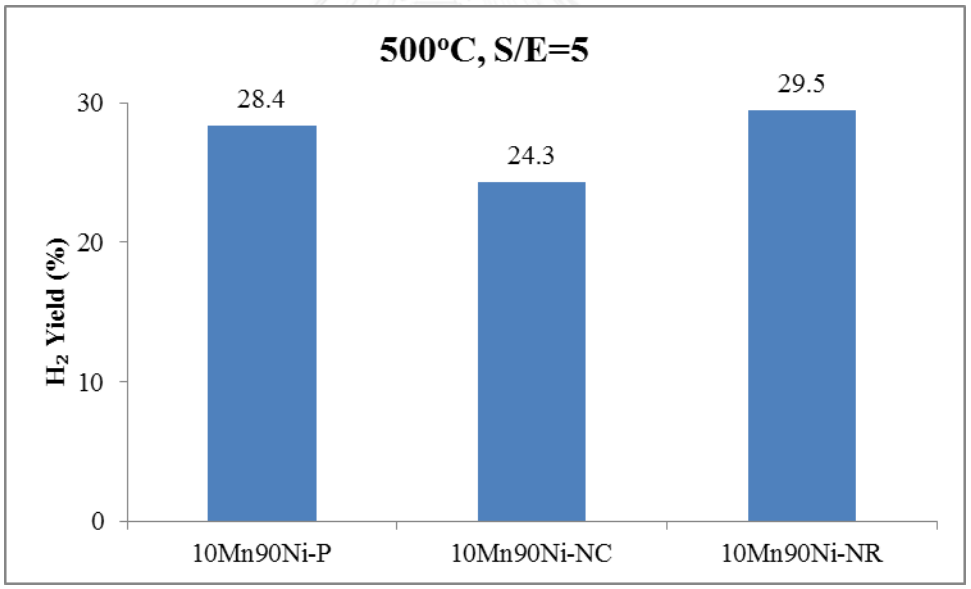

Figure 24: H_2 yields of 10Mn90Ni catalysts supported on different ceria morphologies at 500°C and S/E ratio of 5

The effect of S/E ratios on H_2 yield is shown in Figure 23 and Figure 24. It is clear that increasing S/E ratio generally raised the amount of H_2 produced from the reforming process. Of the catalysts investigated, the one supported on ceria nanorods showed the highest H_2 yield at high S/E ratios. This is because this type of support could create considerable amounts of oxygen vacancies, as mentioned in

previous parts, and those vacancies could act as adsorption sites for water molecules in the WGS reaction, thereby promoting the production of H_2 [31].

The mass losses of spent catalysts derived from TGA analysis are shown in Table 15. Under the same reaction conditions (temperature of 600°C and S/E ratio of 3), the mass loss of the catalyst supported on ceria nanorods had by far the highest mass loss, at 4.459%, whereas the spent catalyst supported on ceria nanocubes lost just 0.6931% in weight. This result indicated that ceria morphology significantly affected the carbon deposition. However, according to Mattos et al. [3], carbon formation sometimes does not correlate directly to the catalyst deactivation; many catalysts still operate for a long period of time despite high amounts of carbon deposition. Those authors mentioned to CH_x species, resulted from the decomposition of either ethanol or acetaldehyde, and proposed some options that these highly active carbon species can select: (a) encapsulate Ni or Co particles, resulting in catalyst degradation, (b) diffuse through the Ni or Co crystallite and nucleate the growth of carbon filaments, or (c) react with O_2 (or H_2O) to produce CO_x species. After the formation of carbon filaments, the active phase (Ni metal particles) situated on top of the carbon filaments could stay exposed to the reactants and gas-phase intermediates. This could explain why the sample supported on ceria nanorods was very active even though it possessed high carbon deposition. Moreover, when the S/E molar ratio increased from 3 to 7, the mass loss of this catalyst decreased significantly, reconfirming the advantages of high steam to ethanol molar ratios.

Table 15: Mass losses of spent catalysts

Sample	Reaction conditions			Mass loss (%)
	Temperature (°C)	S/E ratio	Reaction time (hours)	
10Mn90Ni/CeO_2-NR	600	3	2.1	4.459
10Mn90Ni/CeO_2-NR	600	7	2.1	0.8895
10Mn90Ni/CeO_2-NC	600	3	2.1	0.6931
10Mn90Ni/CeO_2-P	600	3	2.1	1.922

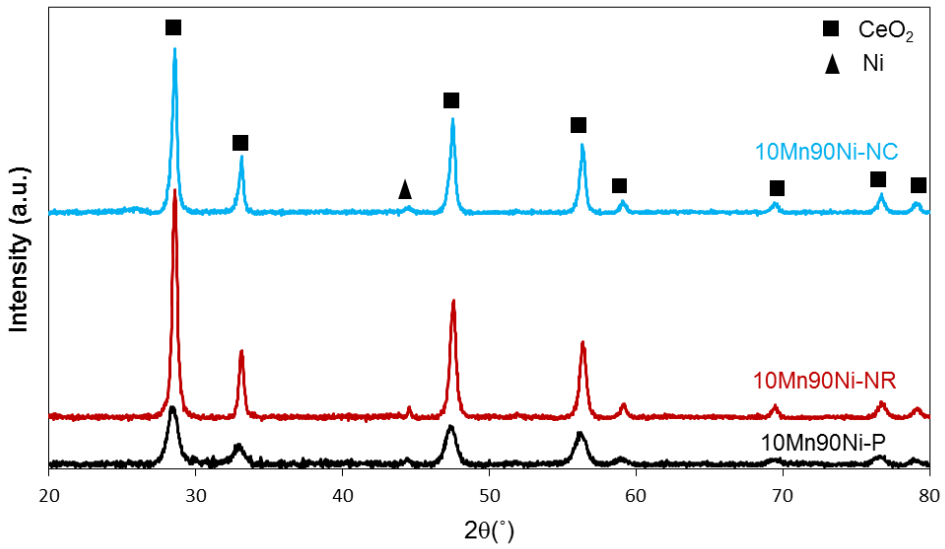

Figure 25: XRD patterns of 10Mn90Ni catalysts after 2 hours of reaction at 600°C, S/E of 3

The XRD patterns of spent 10Mn90Ni catalysts are depicted in Figure 25. Besides the diffraction peaks of ceria with cubic structure, the reflection corresponding to metallic Ni phase could be witnessed at 2θ = 44.5°. The lines of NiO phase completely disappeared, implying that all NiO species were reduced totally by the H_2 reduction step and/or the reduction during the reforming process. In addition, the diffraction line of the sample supported on ceria nanorods became more intense after the reaction, compared to that of the fresh catalyst. This was

consolidated by the crystalline sizes obtained from Scherrer equation (Table 16). For the 10Mn90Ni-NR, the crystallite sizes of CeO_2 and Ni after reaction were much larger than those of CeO_2 and NiO before reaction, suggesting that sintering occurred over this catalyst. The catalyst supported on polycrystalline ceria had the lowest crystalline sizes of CeO_2 and Ni, which indicated that this sample did not undergo sintering. The extent of catalyst sintering over the sample with ceria nanocubes was not considerable.

Table 16: Crystallite sizes of CeO_2, NiO and Ni calculated by Scherrer equation

Sample	d (nm) before reaction		d (nm) after reaction	
	CeO_2[a]	NiO[b]	CeO_2[a]	Ni[b]
10Mn90Ni/CeO_2-P	16	27	13	18
10Mn90Ni/CeO_2-NR	21	14	26	55
10Mn90Ni/CeO_2-NC	60	14	43	18

[a] calculated by using the (111) ceria plane

[b] calculated by using the (200) NiO plane

Optimization by FCCCD-RSM analysis

After screening the significant factors with the factorial design, a FCCCD-RSM (face-centered central composite-response surface methodology) was utilized to figure out the optimum conditions for maximal hydrogen yield. Based on the significance of the four main factors in influencing hydrogen yield outcomes, three independent factors were chosen, namely temperature (A), morphology (B) and S/E ratio (C). The levels of selected factors were similar to those in the factorial design described above, whilst the W/F ratio was kept constant at 22.44 g_{cat}h/mole EtOH for all runs. The specific design matrix is shown in Table 17. The hydrogen yield response surface equation in terms of coded factors can be expressed as follows:

$$Y_{H_2}(\%) = 29.62 + 9.72A + 1.80B + 4.78C - 0.60AB + 0.75AC + 1.38BC + 1.16A^2 - 3.54B^2 - 1.44C^2$$

The R-squared (0.9880) obtained from the ANOVA (Table 18) indicated a good agreement between observed values for hydrogen yield and estimated counterparts. The discrepancy between Adj. R-squared (0.9726) and that of R-squared was very small, which revealed the presence of a requisite term in the model. The RSM model could clarify just over 97% of the response variability. Adequate precision is basically a measure of signal to noise ratio, the desired value of which should be greater than 4. In this case, the ratio of 28.409 was much higher than 4, and this indicates an adequate signal. The above facts could prove that the model is acceptable, and that the model could be utilized to navigate the design space.

Table 17: Experimental variables in coded values for the FCCCD-RSM with three central points

Standard order	Run order	A	B	C	Hydrogen yield (%)
1	7	-1	-1	-1	13.2
2	8	1	-1	-1	28.9
3	3	-1	1	-1	11.1
4	4	1	1	-1	30.0
5	5	-1	-1	1	23.6
6	6	1	-1	1	43.1
7	1	-1	1	1	16.8
8	2	1	1	1	37.9
9	17	-1	0	0	20.7
10	9	1	0	0	42.7
11	11	0	-1	0	29.5
12	10	0	1	0	24.5
13	16	0	0	-1	24.3
14	15	0	0	1	33.9
15	12	0	0	0	28.6
16	13	0	0	0	28.2
17	14	0	0	0	28.4

Table 18: Analysis of variance (ANOVA) of the significant terms for the FCCCD-RSM with three central points.

Source	Sum of Squares	DF	Mean square	F value	P-value
Model	1290.94	9	143.44	64.07	< 0.0001
A-Temperature	944.78	1	944.78	422.04	< 0.0001
B-Morphology	32.4	1	32.40	14.47	0.0067
C-S/E ratio	228.48	1	228.48	102.06	< 0.0001
AB	2.88	1	2.88	1.29	0.2940
AC	4.5	1	4.50	2.01	0.1992
BC	15.13	1	15.13	6.76	0.0355
A^2	3.61	1	3.61	1.61	0.2448
B^2	33.56	1	33.56	14.99	0.0061
C^2	5.55	1	5.55	2.48	0.1593
Residual	15.67	7	2.24		
Lack of Fit	15.59	5	3.12	77.95	0.0127
Pure Error	0.08	2	0.04		
Cor Total	1306.61	16			
R-Squared	0.9880		C.V. %	5.47	
Adj R-Squared	0.9726		Adeq	28.409	

In order to find out the optimum condition for hydrogen yield, the 3D response surface curves were constructed (Figure 26). From those figures, the required condition for the maximum hydrogen yield, estimated by the surface analysis, was 600°C with S/E ratio of 7 and W/F ratio of 22.44 g_{cat}h/mole EtOH using the catalysts supported on ceria nanorods. Under such condition, the experimental hydrogen yield observed was 43.1%, which was very close to the FCCCD-RSM derived value, at 43.6%.

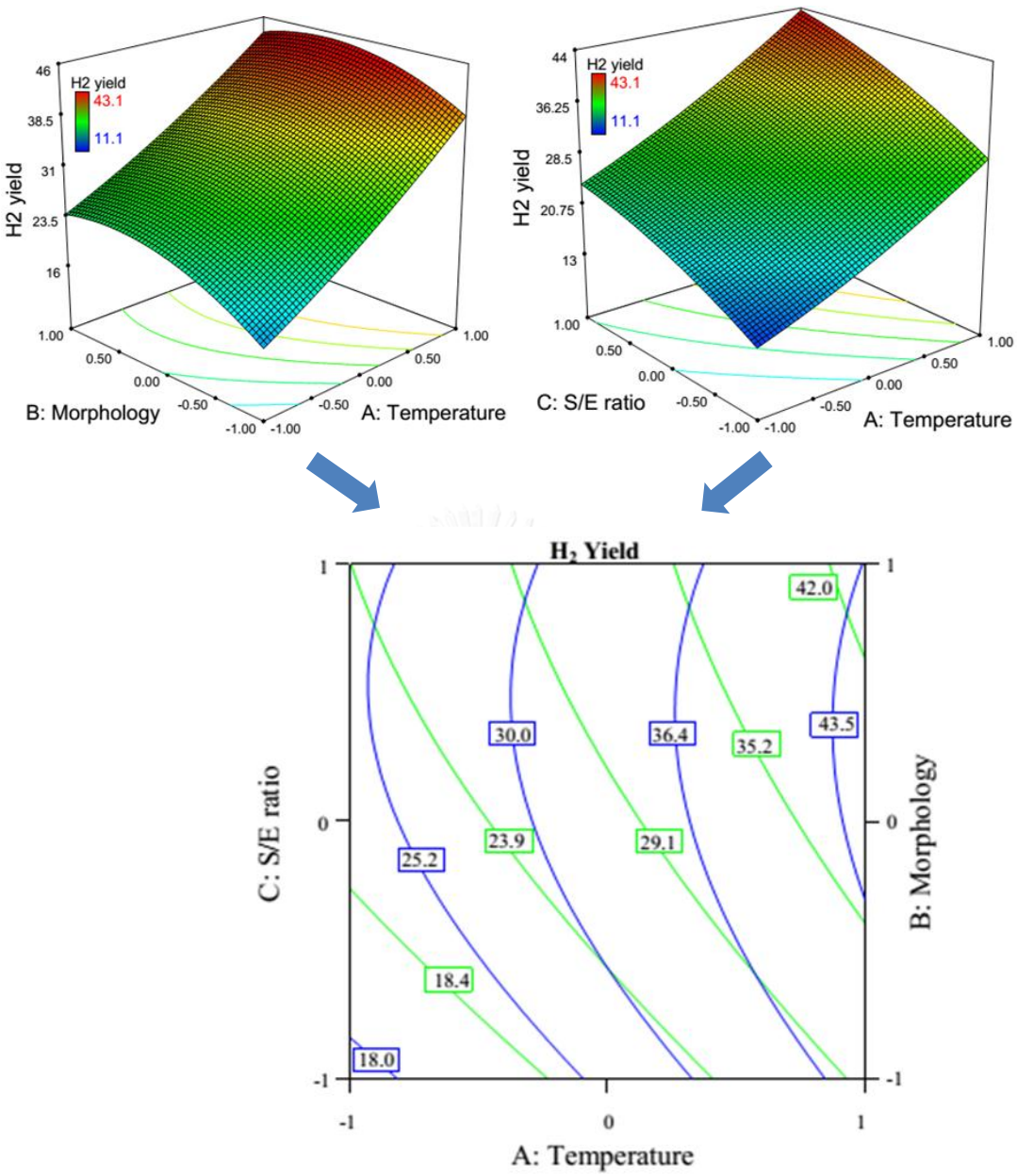

Figure 26: Face-centered central composite response surface plots of (a) A & B effects with S/E ratio of 7 and W/F ratio of 22.44 gcath/mole EtOH and (b) A & C effects with ceria nanorods and W/F ratio of 22.44 gcath/mole EtOH

Four more experiments with different parameters were conducted in order to inspect the accuracy of the model (see Table 19). As can be seen, the experimental hydrogen yield values were very close to estimated counterparts. This signified that the model appeared acceptable and satisfied.

Table 19: Validation of the FCCCD-RSM

A: Temperature	B: Morphology	C: S/E ratio	Estimated Hydrogen yield (%)	Experimental Hydrogen yield (%)
600°C	Nanocubes	5	35.8	38.8
600°C	Nanorods	5	38.1	39.9
600°C	Polycrystalline	5	40.5	40.4
600°C	Polycrystalline	3	33.5	32.2

CHAPTER 5: CONCLUSIONS AND RECOMMENDATIONS

5.1. Conclusions for the first phase

Three series of nickel-based catalysts supported on ceria, namely Ni-Mn/CeO_2-P, Ni-Cu/CeO_2-P and Ni-Cu-Mn/CeO_2-P, were successfully synthesized by means of precipitation and incipient wetness impregnation methods. The catalytic activity of those catalysts for producing hydrogen via ethanol steam reforming was then studied under atmospheric pressure, reaction temperature of 400^{o}C, S/E ratio of 3 and W/F ratio of 22.44g_{cat}h/$mole_{ethanol}$. Of the samples investigated, the ones with higher copper loadings created larger amounts of hydrogen, but the accompanied quantities of undesired and harmful products such as CO, CH_3CHO, CH_3COCH_3 and C_2H_4 were also considerably great. This indicated that dehydrogenation and dehydration reactions were favored on such catalysts. Moreover, XRD and TPR results also revealed that copper species tended to agglomerate together to form larger clusters, which made copper-containing catalysts less reducible. By contrast, Mn ions entered into the lattice of ceria to prevent the strong interaction between active phase (nickel) and the support, and this tremendously improved the reducibility of Ni-Mn/CeO_2-P catalysts. Moreover, the unification of Mn cations into the ceria lattice enabled more oxygen vacancies to be produced, thereby to some extent promoting the catalytic performance during the reforming process. What is more, the main products generated by this series of catalysts were only H_2, CO, CO_2 and CH_4, suggesting that ethanol decomposition and water gas shift reactions dominated the reaction pathways. Among the catalysts examined, 10Mn90Ni/CeO_2-P exhibited relatively outstanding catalytic performance with regard to ethanol conversion, hydrogen yield and product distribution. This loading, therefore, was chosen for the second phase.

5.2. Conclusions for the second phase

From the statistical analysis gained from a full 2^4 factorial design, the factors that had important influence on hydrogen yield were temperature, ceria morphology and S/E molar ratio. Increasing reaction temperature increased the amount of hydrogen yielded since steam reforming reactions of methane and acetaldehyde were thermodynamically favored. Similarly, higher S/E ratio brought higher quantity of water molecules in the feed stream, which encouraged WGS and steam reforming reactions. As a result, more hydrogen was formed.

For ceria morphology, the catalyst supported on conventional polycrystalline ceria showed better activity at low temperature and S/E ratio, whereas those supported on ceria nanorods and nanocubes were more active at higher temperatures and S/E ratios, as proved in the XRD and TPR sections. From the FCCCD-RSM analysis, the optimum condition for maximal hydrogen yield was reaction temperature of 600°C, S/E ratio of 7 and using ceria nanorods as the support. Under such condition, the experimental hydrogen yield was 43.1%, which was in good agreement with the estimated value, at 43.6%.

5.3. Recommendations

In order to obtain high hydrogen yield from ethanol steam reforming, the entire process should be carried out at high reaction temperature to facilitate steam reforming reaction. However, this parameter should not be set at too high values since the WGS equilibrium will be shifted backward to more CO. Besides, excessive concentration of water in the inlet stream will favor steam reforming reactions, thereby increasing hydrogen yield. Too much water in the ethanol solution, on the other hand, requires more energy to vaporize the liquid mixture and thus remarkably increase the operation cost. Furthermore, H_2O molecules may predominate over the adsorption stage, reducing the number of available active sites for other reactants. Therefore, suitable S/E ratio must be carefully considered to satisfy both economic and performance requirements.

Regarding catalysts for the ethanol steam reforming, nickel should be utilized as the active components, and Mn could play the role of a promoter in improving reducibility and oxygen vacancies. Ceria nanorods and nanocubes may be the suitable support for the ESR catalyst, and this is likely due to the fact that those ceria morphology are really active at high temperatures. In addition, ceria nanocubes and nanorods can produce remarkable amounts of oxygen vacancies, on which the dissociative adsorption of water occurs. This could promote the WGS reaction, partly contributing to a better ESR catalytic activity.

REFERENCES

[1] J.L. Contreras, J. Salmones, J.A. Colin - Luna, L. Nuno, B. Quintana, I. Cordova, B. Zeifert, C. Tapia, and G.A. Fuentes, *Catalyst for H_2 production using the ethanol steam reforming (a review).* International Journal Hydrogen Energy, 39 (**2014**) 18835 - 18853.

[2] Meng Ni, Dennis Y.C. Leung, and Micheal K.H. Leung, *A review on reforming bio - ethanol for hydrogen production.* International Journal Hydrogen Energy, 32 (**2007**) 3238 - 3247.

[3] Lisiane V. Mattos, Gary Jacobs, Burtron H. Davis, and Fábio B. Noronha, *Production of Hydrogen from Ethanol: Review of Reaction Mechanism and Catalyst Deactivation.* Chemical Reviews, 112 (**2012**) 4094 - 4123.

[4] Velu Subramani, Pradeepkumar Sharma, Lingzhi Zhang, and Ke Liu, *Hydrogen and Syngas Production and Purification Technologies*, ed. K. Liu, C. Song, and V. Subramani. 2010, New Jersey, US: John Wiley & Sons, Inc.,.

[5] Tengfei Hou, Bo Yu, Shaoyin Zhang, Tongkuan Xu, Dazhi Wang, and WeijieCai, *Hydrogen production from ethanol steam reforming over Rh/CeO_2 catalyst.* Catalysis Communications, 58 (**2015**) 137 - 140.

[6] P. Ciambelli, V. Palma, and A. Ruggiero, *Low temperature catalytic steam reforming of ethanol. 1. The effect of the support on the activity and stability of Pt catalysts.* Applied Catalysis B: Environmental, 96 (**2010**) 18 -27.

[7] Jie Sun, Xin-Ping Qiu, Feng Wu, and Wen-Tao Zhu, *H_2 from steam reforming of ethanol at low temperature over Ni/Y_2O_3, Ni/La_2O_3 and Ni/Al_2O_3 catalysts for fuel-cell application.* International Journal Hydrogen Energy, 30 (4) (**2005**) 437 - 445.

[8] Hua Song, Lingzhi Zhang, Rick B. Watson, Drew Braden, and Umit S. Ozkan, *Investigation of bio-ethanol steam reforming over cobalt-based catalysts.* Catalysis Today, 129 (3 - 4) (**2007**) 346 - 354.

[9] Li-Chung Chen and Shawn D. Lin, *The ethanol steam reforming over $Cu-Ni/SiO_2$ catalysts: Effect of Cu/Ni ratio.* Applied Catalysis B: Environmental, 106 (**2011**) 639 - 649.

[10] E.C. Wanat, K. Venkataraman, and L.D. Schmidt, *Steam reforming and water–gas shift of ethanol on Rh and Rh–Ce catalysts in a catalytic wall reactor.* Applied Catalysis A: General, 276 (**2004**) 155-162.

[11] Tarak Mondal, Kamal K. Pant, and Ajay K. Dalai, *Catalytic oxidative steam reforming of bio-ethanol for hydrogen production over Rh promoted Ni/CeO_2-ZrO_2 catalyst.* International Journal of Hydrogen Energy, 40 (**2015**) 2529-2544.

[12] Xiaxia Zhao and Gongxuan Lu, *Modulating and controlling active species dispersion over Ni-Co bimetallic catalysts for enhancement of hydrogen production of ethanol steam reforming.* International Journal of Hydrogen Energy, 41 (**2016**) 3349-3362.

[13] Ali Hedayati, Olivier Le Corre, Bruno Lacarrière, and Jordi Llorca, *Experimental and exergy evaluation of ethanol catalytic steam reforming in a membrane reactor.* Catalysis Today, 268 (**2016**) 68–78.

[14] Karan D. Dewoolkar and Prakash D. Vaidya, *Tailored hydrotalcite-based hybrid materials for hydrogen production via sorption-enhanced steam reforming of ethanol.* International Journal of Hydrogen Energy, 41 (**2016**) 6094-6106.

[15] Sahar Chitsazan, Soodeh Sepehri, Gabriella Garbarino, Maria M. Carnasciali, and Guido Busca, *Steam reforming of biomass-derived organics: Interactions of different mixture components on Ni/Al_2O_3 based catalysts.* Applied Catalysis B: Environmental, 187 (**2016**) 386-398.

[16] Paula Osorio-Vargas, Nicolás A. Flores-González, Rufino M. Navarro, Jose L.G. Fierro, Cristian H. Campos, and Patricio Reyes, *Improved stability of Ni/Al_2O_3 catalysts by effect of promoters (La_2O_3, CeO_2) for ethanol steam-reforming reaction.* Catalysis Today, (**2015**).

[17] Asawin Bampenrat, Vissanu Meeyoo, Boonyarach Kitiyanan, Pramoch Rangsunvigit, and Thirasak Rirksomboon, *Naphthalene steam reforming over Mn-doped CeO_2–ZrO_2 supported nickel catalysts.* Applied Catalysis A: General, 373 (**2010**) 154 - 159.

[18] N.J. Divins, A. Casanovas, W. Xu, S.D. Senanayake, D. Wiater, A. Trovarelli, and J. Llorca, *The influence of nano-architectured CeO_x supports in $RhPd/CeO_2$ for the catalytic ethanol steam reforming reaction.* Catalysis Today, 253 (**2015**) 99 -105.

[19] I. Ilgaz Soykal, Burcu Bayram, Hyuntae Sohn, Preshit Gawade, Jeffrey T. Miller, and Umit S. Ozkan, *Ethanol steam reforming over Co/CeO_2 catalysts: Investigation of the effect of ceria morphology.* Applied Catalysis A: General, 449 (**2012**) 47 - 58.

[20] Lihong Huang, Fangbai Zhang, Rongrong Chen, and Andrew T. Hsu, *Manganese-promoted nickel/alumina catalysts for hydrogen production via auto-thermal reforming of ethanol.* International Journal Hydrogen Energy, 37 (**2012**) 15908 - 15913.

[21] F. Marino, M. Boveri, G. Baronetti, and M. Laborde, *Hydrogen production fromsteamreforming of bioethanol using $Cu/Ni/K/\gamma$-Al_2O_3 catalysts. Effect of Ni.* International Journal Hydrogen Energy, 26 (**2001**) 665 - 668.

[22] Seung Won Jo, Byeong Sub Kwak, Kang Min Kim, Jeong Yeon Do, No-Kuk Park, Tae Jin Lee, Sang-Tae Lee, and Misook Kang, *Reasonable harmony of Ni and Mn in core@shell-structured $NiMn@SiO_2$ catalysts prepared for hydrogen production from ethanol steam reforming.* Chemical Engineering Journal, 288 (**2016**) 858-868.

[23] Tamara Siqueira Moraes, Raimundo Crisostomo Rabelo Neto, Mauro Celso Ribeiro, Lisiane Veiga Mattos, Marios Kourtelesis, Xenophon Verykios, and Fabio B. Noronha, *Effects of Ceria Morphology on Catalytic Performance of Ni/CeO_2 Catalysts for Low Temperature Steam Reforming of Ethanol.* Topics in Catalysis, 58 (**2015**) 281–294.

[24] Gongshin Qi, Ralph T. Yang, and Ramsay Chang, *MnO_x-CeO_2 mixed oxides prepared by co-precipitation for selective catalytic reduction of NO with NH_3 at low temperatures.* Applied Catalysis B: Environmental, 51 (**2004**) 93 - 106.

[25] Ali Behrad Vakylabad, Mahin Schaffie, AliNaseri, Mohammad Ranjbar, and ZahraManafi, *A procedure for processing of pregnant leach solution (PLS) produced from a chalcopyrite-ore bio-heap: CuO Nano-powder fabrication.* Hydrometallurgy, 163 (**2016**) 24-32.

[26] WANG Hong, ZHANG Lijuan, LI Miao, LIU Yuan, and BAI Xue, *Co/CeO_2 for ethanol steam reforming: effect of ceria morphology.* JOURNAL OF RARE EARTHS, 31 (**2013**) 565.

[27] Qihai LIU, Zili LIU, Xinhua ZHOU, Cuijin LI, and Jiao DING, *Hydrogen production by steam reforming of ethanol over copper doped Ni/CeO_2 catalysts.* JOURNAL OF RARE EARTHS, Vol. 29 (9) (**Sep. 2011**) 872.

[28] G. Blanco, M. A. Cauqui, J. J. Delgado, A. Galtayries, J. A. P´ erez-Omil, and J. M. Rodr´ıguez-Izquierdo, *Preparation and characterization of Ce–Mn–O composites with applications in catalytic wet oxidation processes.* Surface and Interface Analysis, 36 (**2004**) 752-755.

[29] Tamara Siqueira Moraes, Raimundo Crisostomo Rabelo Neto, Mauro Celso Ribeiro, Lisiane Veiga Mattos, Marios Kourtelesis, Spyros Ladas, Xenophon Verykios, and Fábio Bellot Noronha, *The study of the performance of PtNi/CeO_2–nanocube catalysts for low temperature steam reforming of ethanol.* Catalysis Today, 242 (**2015**) 35-49.

[30] Hao-Xin Mai, Ling-Dong Sun, Ya-Wen Zhang, Rui Si, Wei Feng, Hong-Peng Zhang, Hai-Chao Liu, and Chun-Hua Yan, *Shape-Selective Synthesis and Oxygen Storage Behavior of Ceria Nanopolyhedra, Nanorods, and Nanocubes.* The Journal of Physical Chemistry B, 109 (**2005**) 24380-24385.

[31] Julia Vecchietti, Adrian Bonivardi, Wenqian Xu, Dario Stacchiola, Juan J. Delgado, Monica Calatayud, and Sebastián E. Collins, *Understanding the Role of Oxygen Vacancies in the Water Gas Shift Reaction on Ceria-Supported Platinum Catalysts.* ACS Catalysis, 4 (**2014**) 2088–2096.

APPENDIX

APPENDIX A

CALCULATION FOR CATALYSTS IMPREGNATION

Ni-Mn/CeO_2-P catalysts

An example of calculation for the 10Mn90Ni/CeO_2-P sample:

Assuming the desired amount of catalyst (after reduction) is 0.7g.

The total metal loading is 12%

$$\Rightarrow m_{Mn} = 10\% \times 12\% \times 0.7 = 0.0084g$$
$$and \quad m_{Ni} = 90\% \times 12\% \times 0.7 = 0.0756g$$

$$\Rightarrow \mathrm{n_{Mn}} = \mathrm{n_{Mn(NO_3)_2.4H_2O}} = \frac{\mathrm{m_{Mn}}}{\mathrm{M_{Mn}}} = \frac{0.0084}{54.948} = 0.000153\,\mathrm{mol}$$

$$\mathrm{m_{Mn(NO_3)_2.4H_2O}} = \mathrm{n_{Mn(NO_3)_2.4H_2O}} \times \mathrm{M_{Mn(NO_3)_2.4H_2O}} =$$
$$0.000153 \times 251.01 = 0.0384\mathrm{g}$$

$$\text{and} \quad \mathrm{n_{Ni}} = \mathrm{n_{Ni(NO_3)_2.6H_2O}} = \frac{\mathrm{m_{Ni}}}{\mathrm{M_{Ni}}} = \frac{0.0756}{58.6934} = 0.001288\,\mathrm{mol}$$

$$\mathrm{m_{Ni(NO_3)_2.6H_2O}} = \mathrm{n_{Ni(NO_3)_2.6H_2O}} \times \mathrm{M_{Ni(NO_3)_2.6H_2O}}$$
$$= 0.001288 \times 290.80 = 0.3746\mathrm{g}$$

$$m_{CeO_2} = 0.7 - (0.0084 + 0.0756) = 0.616g$$

The similar method of calculation is then applied to the other samples, and the results are listed in the Table A-1 below.

Table A-1: Amounts of precursors corresponding to each sample of the Ni-Mn series

Sample	$m_{Mn(NO_3)_2.4H_2O}$ (g)	$m_{Ni(NO_3)_2.6H_2O}$ (g)	m_{CeO_2} (g)
100Ni	0	0.4162	0.616
10Mn90Ni	0.0384	0.3746	0.616
20Mn80Ni	0.0768	0.3329	0.616
30Mn70Ni	0.1151	0.2913	0.616
50Mn50Ni	0.1919	0.2081	0.616

Ni-Cu/CeO_2-P catalysts

An example of calculation for the 10Cu90Ni/CeO_2-P sample:

Assuming the desired amount of catalyst (after reduction) is also 0.7g.

The total metal loading is still 12%

$$\Rightarrow m_{Cu} = 10\% \times 12\% \times 0.7 = 0.0084g$$
$$and \;\; m_{Ni} = 90\% \times 12\% \times 0.7 = 0.0756g$$

$$\Rightarrow \mathrm{n_{Cu}} = \mathrm{n_{Cu(NO_3)_2.4H_2O}} = \frac{\mathrm{m_{Cu}}}{\mathrm{M_{Cu}}} = \frac{0.0084}{63.546} = 0.000132\,\mathrm{mol}$$

$$\mathrm{m_{Cu(NO_3)_2.3H_2O}} = \mathrm{n_{Cu(NO_3)_2.3H_2O}} \times \mathrm{M_{Cu(NO_3)_2.3H_2O}}$$
$$= 0.000132 \times 241.60 = 0.0319\mathrm{g}$$

$$\text{and} \;\; \mathrm{n_{Ni}} = \mathrm{n_{Ni(NO_3)_2.6H_2O}} = \frac{\mathrm{m_{Ni}}}{\mathrm{M_{Ni}}} = \frac{0.0756}{58.6934} = 0.001288\,\mathrm{mol}$$

$$\mathrm{m_{Ni(NO_3)_2.6H_2O}} = \mathrm{n_{Ni(NO_3)_2.6H_2O}} \times \mathrm{M_{Ni(NO_3)_2.6H_2O}} = 0.001288 \times 290.80$$
$$= 0.3746\mathrm{g}$$

$$m_{CeO_2} = 0.7 - (0.0084 + 0.0756) = 0.616g$$

The similar method of calculation is then applied to the other samples, and the results are listed in the Table A-2 below.

Table A-2: Amounts of precursors corresponding to each sample of the Ni-Cu series

Sample	$m_{Cu(NO_3)_2.3H_2O}$ (g)	$m_{Ni(NO_3)_2.6H_2O}$ (g)	m_{CeO_2} (g)
10Cu90Ni	0.0319	0.3746	0.616
20Cu80Ni	0.0639	0.3329	0.616
30Cu70Ni	0.0958	0.2913	0.616
50Cu50Ni	0.1597	0.2081	0.616

Ni-Cu-Mn/CeO_2-P catalysts

An example of calculation for the Ni10Cu90Mn/CeO_2-P sample:

Assuming the desired amount of catalyst (after reduction) is also 0.7g.

The total metal loading is still 12%, but this time the amount of nickel is kept constant at 6% in all samples. The other 6% is allocated to both Cu and Mn

$$\Rightarrow m_{Ni} = 6\% \times 1 = 0.06g$$

$$\Rightarrow n_{Ni} = n_{Ni(NO_3)_2.6H_2O} = \frac{m_{Ni}}{M_{Ni}} = \frac{0.006}{58.6934} = 0.001022\,mol$$

$$\mathrm{m}_{\mathrm{Ni(NO_3)_2.6H_2O}} = \mathrm{n}_{\mathrm{Ni(NO_3)_2.6H_2O}} \times \mathrm{M}_{\mathrm{Ni(NO_3)_2.6H_2O}} = 0.001022 \times 290.80$$

$$= 0.2973$$

$$\Rightarrow m_{Cu} = 10\% \times 6\% \times 1 = 0.006g$$

$$and\ \ m_{Mn} = 90\% \times 6\% \times 1 = 0.054g$$

$$\Rightarrow n_{Cu} = n_{Cu(NO_3)_2.4H_2O} = \frac{m_{Cu}}{M_{Cu}} = \frac{0.006}{63.546} = 9.44 \times 10^{-5}\,mol$$

$$m_{Cu(NO_3)_2.3H_2O} = n_{Cu(NO_3)_2.3H_2O} \times M_{Cu(NO_3)_2.3H_2O} = 9.44 \times 10^{-5} \times 241.60 = 0.0228g$$

$$\Rightarrow n_{Mn} = n_{Mn(NO_3)_2.4H_2O} = \frac{m_{Mn}}{M_{Mn}} = \frac{0.054}{54.948} = 0.000983\,mol$$

$$m_{Mn(NO_3)_2.4H_2O} = n_{Mn(NO_3)_2.4H_2O} \times M_{Mn(NO_3)_2.4H_2O} = 0.000983 \times 251.01 = 0.2467g$$

$$m_{CeO_2} = 1 - (0.06 + 0.006 + 0.054) = 0.88g$$

The similar method of calculation is then applied to the other samples, and the results are listed in the Table A-3 below.

Table A-3: Amounts of precursors corresponding to each sample of the Ni-Cu-Mn series

Sample	$m_{Ni(NO_3)_2.6H_2O}$ (g)	$m_{Cu(NO_3)_2.3H_2O}$ (g)	$m_{Mn(NO_3)_2.4H_2O}$ (g)	m_{CeO_2} (g)
Ni10Cu90Mn	0.2973	0.0228	0.2467	0.88
Ni30Cu70Mn	0.2973	0.0684	0.1919	0.88
Ni50Cu50Mn	0.2973	0.1141	0.1371	0.88
Ni70Cu30Mn	0.2973	0.1597	0.0822	0.88
Ni90Cu10Mn	0.2973	0.2053	0.0274	0.88

APPENDIX B

CALCULATION FOR ETHANOL CONVERSION, HYDROGEN YIELD AND PRODUCTS SELECTIVITY

Calculation for the ethanol solutions

In order to prepare 25ml ethanol solution with S/E molar ratio of 3, 12ml deionized water and 13ml absolute ethanol were mixed together because of this method of calculation:

$$d_{C_2H_5OH} = 0.79g/ml, d_{H_2O} = 1g/ml$$

Let x_1 and x_2 are the amounts of water and ethanol (in mole), respectively.

$$\Rightarrow \begin{cases} x_1 = 3x_2 \\ V_{H_2O} + V_{C_2H_5OH} = 25 \end{cases} \Rightarrow \begin{cases} x_1 - 3x_2 = 0 \\ \frac{18}{1}x_1 + \frac{46}{0.79}x_2 = 25 \end{cases}$$

$$\Rightarrow \begin{cases} x_1 = 0.6683mol \\ x_2 = 0.2228mol \end{cases} \Rightarrow \begin{cases} V_{H_2O} = 12ml \\ V_{C_2H_5OH} = 13ml \end{cases}$$

So, there would be $\frac{0.2228}{25} = 0.008912mol$ of ethanol in 1ml of ethanol solution

Table B-1 below shows the equivalent amounts of water and ethanol for the other 2 ethanol solutions, namely the ones with S/E ratio of 5 and 7.

Table B-1: Volumes of water and ethanol (ml) corresponding to each ethanol solution

S/E molar ratio	Volume of water (ml)	Volume of ethanol (ml)	Amount of ethanol in 1ml of the solution
3	12.00	13.00	0.008912
5	15.18	9.82	0.006748
7	17.10	7.90	0.005428

An example of calculation for one experiment in the second phase (the experiment with the standard order of 16 and other specific parameters are as follows: 10Mn90Ni/CeO_2-NR, 600°C, S/E = 7, and W/F = 22.44g_{cat}h/$mole_{ethanol}$):

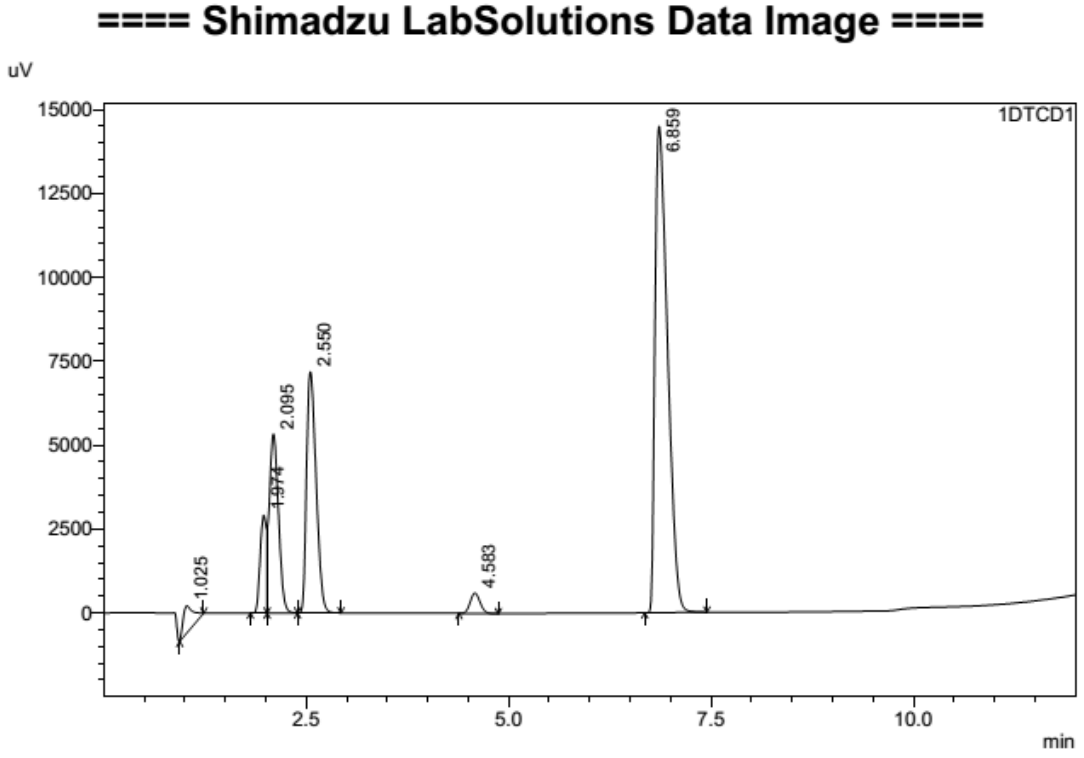

Figure B- 1: The chromatogram derived from the GC

The average analyzed composition of the stream containing non-condensable components is listed in the Table B-2 below.

Table B-2: Data obtained from the GC for the gaseous products from the experiment

Retention Time (min)	Measured area	Standard area	Measured area/Standard area	Name
1.025	7672.0	645	11.9	H_2
2.550	62476.7	13064	4.8	CO
4.583	6111.3	25975	0.2	CH_4
6.859	150523.7	35433	4.2	CO_2

$$\Rightarrow \%vol_{H_2} = \frac{11.9}{11.9+4.8+0.2+4.2} \times 100 = 56.2\%$$

Similarly, proportions (%vol) of CO, CH_4 and CO_2 are 22.6%, 1.1% and 20.1% respectively.

Reaction time: 2.14 hours; flow rate of the gaseous products stream: 10.1ml/min

Flow rate of ethanol solution: 1ml/h

$$\Rightarrow n_{inlet\ ethanol} = 0.005428 \times 2.14 = 0.01162 mol$$

Molar flow rate of products: $\frac{10.1}{[0.082 \times (30+273)]} = 0.4065 mmol/\min$

$$n_{H_2} = 0.4065 \times 2.14 \times 60 \times 56.2\% = 29.33 mmol$$
$$n_{CO} = 0.4065 \times 2.14 \times 60 \times 22.6\% = 11.80 mmol$$
$$n_{CH_4} = 0.4065 \times 2.14 \times 60 \times 1.1\% = 0.58 mmol$$
$$n_{CO_2} = 0.4065 \times 2.14 \times 60 \times 20.1\% = 10.46 mmol$$

Data from liquid GC indicated that there was neither ethanol nor acetaldehyde nor acetone in the liquid collected from the condenser. Hence, the ethanol conversion for this run was 100%.

So,

$$Y_{H_2} = \frac{moles_{H_2},out}{6(moles_{EtOH,in})} \times 100 = \frac{29.33 \times 10^{-3}}{6 \times 0.01162} \times 100 = 42.1\%$$

$$S_{CO} = \frac{moles_{CO}/2}{(moles_{EtOH,in} - moles_{EtOH,out})} \times 100 = \frac{11.80 \times 10^{-3}}{2 \times 0.01162} \times 100 = 50.8\%$$

$$S_{CH_4} = \frac{moles_{CH_4}/2}{(moles_{EtOH,in} - moles_{EtOH,out})} \times 100 = \frac{0.58 \times 10^{-3}}{2 \times 0.01162} \times 100 = 2.5\%$$

$$S_{CO_2} = \frac{moles_{CO_2}/2}{(moles_{EtOH,in} - moles_{EtOH,out})} \times 100 = \frac{10.46 \times 10^{-3}}{2 \times 0.01162} \times 100 = 45.1\%$$

The identical method was applied to other experiments and the results are listed in the tables below.

Table B- 3: Results from the Ni-Cu series in the first phase

Products	10Cu90Ni	20Cu80Ni	30Cu70Ni	50Cu50Ni
X_{EtOH} [%]	98.93	99.43	99.39	96.13
Y_{H_2} [%]	18.48	15.95	14.54	39.39
% Selectivity				
CO	5.28	8.63	14.06	42.36
CH_4	60.89	54.44	49.19	13.48
CO_2	32.55	35.89	35.90	30.40
C_2H_4	-	-	-	4.51
C_2H_6	-	0.15	0.20	-
CH_3COCH_3	-	-	-	4.05
CH_3CHO	-	-	-	1.96

Table B- 4: Results from the Ni-Cu-Mn series in the first phase

Products	Ni10Cu90M	Ni30Cu70M	Ni50Cu50M	Ni70Cu30M	Ni90Cu10M
X_{EtOH} [%]	99.13	98.36	95.93	98.37	91.19
Y_{H_2} [%]	15.44	15.08	29.40	11.93	21.28
% Selectivity					
CO	49.47	48.36	48.78	42.95	42.74
CH_4	18.62	18.70	12.84	24.40	15.13
CO_2	28.69	24.69	29.51	27.10	27.97
C_2H_4	-	-	1.05	-	0.31
CH_3COCH_3	1.24	1.90	2.54	1.98	4.06
CH_3CHO	-	1.26	2.06	1.56	7.41

Table B-5: The design matrix and Ethanol Conversion response data in the second phase

Standard order	Coded factors				Ethanol conversion (%)	
	A	B	C	D	Replicate 1	Replicate 2
1	-	-	-	-	98	98.5
2	+	-	-	-	97.8	97.9
3	-	+	-	-	98	98.1
4	+	+	-	-	98.2	98.3
5	-	-	+	-	100	100
6	+	-	+	-	100	100
7	-	+	+	-	100	100
8	+	+	+	-	100	100
9	-	-	-	+	98.4	98.8
10	+	-	-	+	97.8	100
11	-	+	-	+	99.8	98.3
12	+	+	-	+	98.2	97.8
13	-	-	+	+	100	97.8
14	+	-	+	+	100	97.9
15	-	+	+	+	100	100
16	+	+	+	+	100	100
17	0	0	0	0	97.9	98
18	0	0	0	0	97.9	98
19	0	0	0	0	98.1	97.9
20	0	0	0	0	98.1	97.9

Table B-6: The design matrix and Hydrogen Yield response data in the second phase

Standard order	Coded factors				Hydrogen yield (%)	
	A	B	C	D	Replicate 1	Replicate 2
1	-	-	-	-	10.43	8.7
2	+	-	-	-	28.4	29.19
3	-	+	-	-	18.4	15.92
4	+	+	-	-	33.72	33.11
5	-	-	+	-	14.11	15.22
6	+	-	+	-	38.25	38
7	-	+	+	-	25.53	22.81
8	+	+	+	-	38.84	42.09
9	-	-	-	+	10.39	11.72
10	+	-	-	+	29.88	30.09
11	-	+	-	+	15.58	10.74
12	+	+	-	+	28.94	28.86
13	-	-	+	+	15.74	17.81
14	+	-	+	+	38.19	37.65
15	-	+	+	+	22.69	24.41
16	+	+	+	+	42.1	44.1
17	0	0	0	0	27.56	28.75
18	0	0	0	0	27.9	30.47
19	0	0	0	0	28.52	30.62
20	0	0	0	0	33.27	30.11

VITA

My name is Huan Nam Tran Dang. I graduated from the Industrial University of Ho Chi Minh City in 2014 with a degree of engineer in chemical engineering. Next, I started to pursue master degree in Department of Chemical Technology, Chulalongkorn University in academic year 2014.

I made an oral presentation at the Pure and Applied Chemistry International Conference, February 2016, Bangkok. The topic was "The activities of manganese promoted nickel-based catalysts supported on ceria for producing hydrogen via ethanol steam reforming", and my proceeding was then accepted to be published in PACCON 2016 proceedings book.